5-2014

Synthesis and Characterization of Nanocrystals and Their Application for Photodetectors

Ahmad Nusir
University of Arkansas, Fayetteville

Synthesis and Characterization of Nanocrystals and Their Application for Photodetectors

Synthesis and Characterization of Nanocrystals and
Their Application for Photodetectors

A thesis submitted in partial fulfillment
of the requirements for the degree of
Master of Science in Electrical Engineering

By

Ahmad I. Nusir
University of Jordan
Bachelor of Science in Electrical Engineering, 2012

May 2014
University of Arkansas

This thesis is approved for recommendation to the Graduate Council

_____
Dr. Omar Manasreh
Thesis Director

_____
Dr. Simon Ang
Committee Member

_____
Dr. Joseph B. Herzog
Committee Member

ABSTRACT

Room temperature operation is considered one of the essential restrictions in the design of electronic devices. Photodetectors are unable to detect light efficiently at room temperature due to high dark currents. Semiconductor nanocrystals possess unique optical and electrical properties which make them ideal for fabricating uncooled photodetectors. In this project, nanocrystals were synthesized and implemented in devices that detect light at room temperature.

Nanocrystalline I-III-VI_2 and II-VI semiconductors ($CuInS_2$ and CdSe) were grown by a wet chemical method, and characterized using: optical absorption, photoluminescence, Raman scattering, and x-ray diffraction. The optical absorption and photoluminescence spectra of the nanocrystals were recorded at different growth reaction times, and showed an increase in the size of the nanocrystals with longer reaction times. The structural properties of $CuInS_2$ nanocrystals were investigated using Raman spectroscopy and x-ray diffraction.

Photodetectors were fabricated by depositing CdSe nanocrystals on interdigitated electrodes with spacing of 5 and 50 μm. The current-voltage curves of the devices showed a low dark current (< 1 nA), and photocurrent higher than the dark current by several orders of magnitude. The room temperature detectivity for the device with 5 μm spacing was extracted from the current-voltage curve and found to be on the order of $3.5x10^{10}$ $cmHz^{1/2}W^{-1}$ at 5 V bias voltage. The onset of the spectral response was positioned at 710 nm, which coincide with the photoluminescence of the nanocrystals. Another type of photodetector was fabricated from semi-insulating GaAs using interdigitated gold electrodes with different spacing (5, 10, 20, and 50 μm). Significant enhancement in the spectral response was observed as the electrode spacing

was reduced from 50 to 5 μm. The spectral response of smaller spacing devices (5 and 10 μm) showed dependence on the polarization of incident light.

The integration of nanocrystals with interdigital metallization simplified the device structure, and improved on its performance by reducing the dark current. Furthermore, the interaction between incident light and gold electrodes produced a plasmonic effect. This plasmonic effect is responsible for the enhancement seen in the spectral response spectra.

ACKNOWLEDGMENTS

I would like to express my deep gratitude to my graduate advisor and thesis director, Dr. Omar Manasreh for providing me the opportunity to do research in Optoelectronics and Nanomaterials Lab. Without his valuable instructions none of the tremendous hard work would be achieved.

Also, I am thankful to Dr. Simon Ang and Dr. Joseph B. Herzog who serve as my committee members and who have made my time here such an intellectual and personal delight

I would like to thank my research group members, Yahia F. Makableh, Ramesh Vasan, Jony Sarker, Dr. Mehemt Sahin, Seungyong Lee, Mohammed Marie, Sanghamitra Mandal, Rick Eyi, and Juan Aguilar, Zack Bever, for their help and support throughout my project. Also, I would like to thank Dr. Mahmoud Khan, Dr. Scott Little and John Dixon for helping me with the synthesis of the nanocrystals.

This work was supported by the Air Force Office of Scientific Research (Grant No. FA9550-10-1-0136), and NASA (Grant No. 242026-1BBX11AQ36A).

DEDICATION

This thesis is dedicated to my parents and my sisters for their help and support. Their valuable advises and wishes helped me to focus on the essentials and continue my graduate career. Without them I would not move this far.

TABLE OF CONTENTS

LIST OF FIGURES

I. INTRODUCTION

Materials and devices at the nano-scale had witnessed great development in the past decades, and became applicable in various fields of science including electronics, biology, and chemistry. Nanomaterial semiconductors, such as, quantum wells, wires, and dots, possess unique optical and electrical properties over bulk semiconductors due to the carrier confinement. [1] Several efforts were made to utilize these properties and enhance the performance of optoelectronic devices. Yet, the field has not reached the expected potentials and still in progress to be further explored.

Semiconductor nanocrystals were intensively investigated and applied in a wide range of optoelectronic devices, such as, solar cells, light-emitting diodes, lasers, and photodetectors. Quantum size effect is one of the unique properties that enables tuning the absorption and emission spectra of the nanocrystals over a wide range. Nanocrystals synthesized via wet chemical method can be dispersed and processed in a solvent, therefore they are suitable for cost effective mass production. Another property owned by the nanocrystals is the quantum tunneling effect that can be implemented in many applications. Recently, researchers were successful in synthesizing high quality nanocrystals with various bandgaps that cover a wide range of the spectral region.

Photodetectors gained huge attentions due to numerous applications, such as, military and defense, space science, and chemical analysis. Nanocrystals arose as a possible candidate to replace quantum wells in the near and mid-infrared detection. They exhibit potentials in detecting normal incident light, low dark currents, room temperature operation, and high photoconductive gain. [2]

Chapter 1 will discuss the basic theory behind colloidal nanocrystals, and their use in detecting light. Chapter 2 is dedicated to the process of growing the nanocrystals, and the fabrication techniques used in building the devices. Chapter 3 will discuss the characterization methods used to characterize both the materials and the devices. Chapter 4 analyses the major results obtained from characterizing the materials and devices. Finally, in chapter 5 the project is concluded and future work is proposed.

A. COLLOIDAL NANOCRYSTALS

Overview

Inorganic semiconductor nanocrystals are classified into three main groups: binary, ternary, and quarternary, depending on the number of elements in each group. These nanocrystals were under intensive study to explore new synthetic routes able to produce nanocrystals with high quality. [6-9] Binary compound nanocrystals are formed from elements belonging to II-VI and IV-VI groups, such as, CdSe, CdTe, and PbS. Several studies were conducted to control the size and shape of these nanocrystals. [10] Although they have excellent optical properties, but the presence of heavy metals (Cd and Pb) is considered extremely dangerous. InAs and InP nanocrystals belonging to III-V Group were used to replace the heavy metals.

Ternary compounds nanocrystals members of I-III-VI_2 group were also investigated, and they are represented by $CuInS_2$ and $CuInSe_2$. In this group, the heavy metals are replaced by the two cations: Cu^{+1} and In^{+3}. Quaternary compound nanocrystals like CZTS have attracted the attentions recently. [11] They are more environmental friendly and less expansive compared to $CuInS_2$, since the indium is replaced by cheaper and more abundant elements: zinc and tin.

Wet chemical method also referred to colloidal growth is one of the efficient approaches that are used to synthesize the nanocrystals. There are two common methods to perform the wet chemical growth: one pot synthesis, and hot injection method. The shape and the size of the nanocrystals can be easily controlled following this approach. [12] Also, the synthesized nanocrystals are dispersed in a solvent, allowing the formation of thin films by non-vacuum deposition techniques, such as drop casting, spray coating, ink-jet printing, dip coating, electrophoretic deposition, and spin coating. These deposition techniques may reduce both the complexity and the cost of the fabricated devices. On the other hand, complicated vacuum methods can be used to grow the nanocrystals' thin films including: sputtering, chemical vapor deposition, and molecular beam epitaxy. Although high quality films can be achieved by these techniques, but they require slower deposition rates, higher cost, and high operating temperatures.[13]

Nanocrystals grown by wet chemical method are usually capped with organic ligands, that are used during the synthesis to control the nucleation and growth of the nanocrystals, and to provide chemical passivation. Such passivation is important to prevent the nanocrystals from aggregation, and subsequently prevent them from being dispersed in solvents. [14] However, these long insulating ligands surrounding the nanocrystals will hamper the transfer of carriers between the nanocrystals. And will affect negatively on the carrier mobility in the formed films. [13] Therefore, long organic ligands are exchanged with shorter and more conducting ones like pyridine, and butylamine. [15] The ligand exchange is performed after the synthesis process, while the nanocrystals are in the liquid phase.

CdSe Nanocrystals

Cadmium selenide (CdSe) nanocrystals have received considerable attentions in the past decades, due to their distinctive optical properties. The absorbance spectra of the nanocrystals can be tuned within the visible spectral region in the wavelength range between 475 and 670 nm. Moreover, high photoluminescence quantum yield was achieved by CdSe nanocrystals. [16] These optical properties made CdSe nanocrystals applicable in different optoelectronic devices, such as, solar cells, [17] photodetectors, [18] and light emitting diodes. [19]

In addition to the size dependent luminescence wavelength, CdSe nanocrystals can exist in two crystalline structures: hexagonal wurtzite, and cubic zincblende that depend on the growth conditions. [20] In the zincblende structure the stacking sequence is repeated every three layers in the <111> direction, while in the wurtzite structure the stacking sequence is repeated every two layers in the <0001> direction. [21] The unit cells of the cubic zincblende and hexagonal wurtzite are shown in figure 1.1 (a) and (b), respectively.

$CuInS_2$ Nanocrystals

Copper indium disulfide nanocrystals are considered as the most promising materials for photovoltaic applications because of their interesting optical properties. First, $CuInS_2$ nanocrystals have a size dependent absorption and photoluminescence spectra, which can be tuned in the visible and near-infrared spectral regions. [22] Second, it has a direct bandgap of 1.5 eV (827 nm) in the bulk material, that matches the incident solar spectrum. [23] Furthermore, their optical absorption coefficient is in the order of 10^{-5} cm^{-1}. This is ten times greater than the absorption coefficient of CdTe nanocrystals. [24] This high absorption coefficient enables absorbing the light within lower thickness of the deposited film.

Cadmium-free nanocrystals were implemented in light energy harvesting systems, [25] and photodetectors. [26] Copper indium disulfide nanocrystals have chalcopyrite lattice structure. This is formed by doubling the zincblende structure along the z-axis and consequently obtaining a tetragonal unit cell with height of *c*, and a square base with side of *a*. The ratio *c*/*a* is close to two as shown in figure 1.1 (c). [27] The copper to indium ratio will determine the type of the semiconductor, excess copper is always p-type. [23]

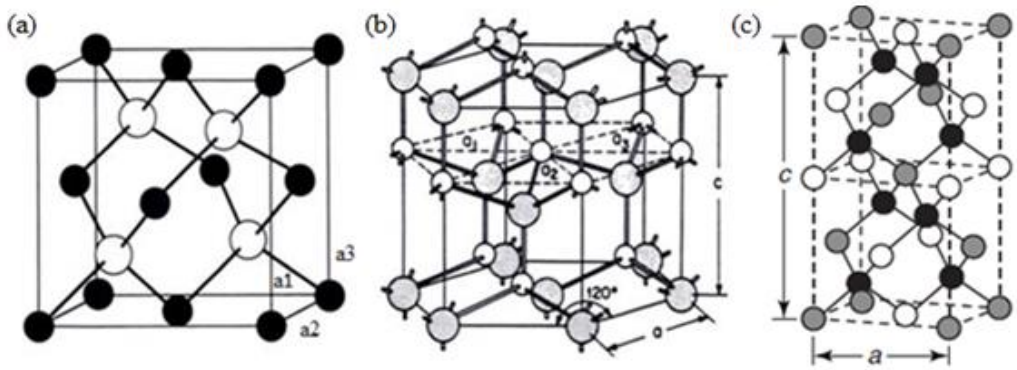

Figure 1.1 (a) Cubic zincblende unit cell. [21] (b) Hexagonal wurtzite unit cell. [21] (c) The unit cell of chalcopyrite lattice structure. [27]

Quantum Confinement in Nanocrystals

Nanocrystals have three dimensions carrier confinement and their structures consist of discretized energy levels. [3] This 3D carrier confinement resembles an electron trapped inside a box. The optical and electrical properties of the nanocrystals are determined by their size and shape. For example, the optical properties of the nanocrystals undergo massive changes as their size decreases. When the size of the nanocrystals reduces, the separation between energy levels becomes larger, and fewer electronic transitions can be obtained. [4] The bandgap of the nanocrystals can be described according to the following equation: [5]

$$\hbar\omega = E_g + x^2 \frac{\pi^2 \hbar^2}{2m_r^* a_o^2} \tag{1.1}$$

where $\hbar$ is the reduced Planck constant, ω is the angular frequency, E_g is the bandgap of bulk materials, x is the reduced photon energy, m_r^* is the reduced effective mass, a_o is the diameter of the nanocrystals. As shown in equation 1.1, the bandgap of the nanocrystals is inversely proportional to the square of the diameter of nanocrystals. As a result, the onset of the optical absorption spectrum can be controlled by the varying the size of the nanocrystals.

B. NANOCRYSTALS FOR PHOTODETECTION

Overview

Photodetectors operating in the ultra-violet, visible region, and near-infrared were fabricated using nanocrystals with suitable bandgap. Ultra-violet photodetectors were fabricated using wide bandgap nanocrystals like ZnO, and TiO_2. [28,29] These photodetectors can be used in many applications like: flame sensing, missile launch detection, and optical communication. Other photodetectors operating in the visible region were fabricated using smaller size PbS nanocrystals, and were used in image sensors. [30] Detection of light in the near-infrared region is possible using nanocrystals with narrow bandgap, such as, InAs and PbSe.

Cadmium selenide nanocrystals with a bandgap of 1.7 eV (730 nm) were implemented in devices that operate in the visible spectral region 475 – 650 nm. [31] It is well known that increasing the size of the synthesized nanocrystals will decrease the bandgap. Therefore, it is possible to detect low energy light up to 730 nm using CdSe nanocrystals. [18] Photodetectors operating in the near-infrared region were fabricated using InAs quantum dots grown by

molecular beam epitaxy. [32] However, the fabricated devices exhibit reduction in the detectivity as the temperature increases, due to the increase in the dark current.

Different configurations of device structure were investigated including p-n hetrojunctions, [33] Schottky contacts with vertical sandwich-like geometry, [31] and planar interdigital metallization. [34] Photodetectors can be fabricated by depositing the dispersed nanocrystals on interdigitated electrodes. This approach will simplify the device structure, and improve the performance by reducing the dark current, due to the formation of Schottky barriers at the interface between metal and semiconductor.

Basics of photoconductors

The operation mechanism of nanocrystals based photodetectors depends mainly on interband transitions that occur within the structure of the nanocrystals. Photons with an energy ($h\nu$) larger than or equal to the bandgap energy (E_g) are absorbed by electrons. The photo-excited electrons jump from the valence band to the conduction band (interband transition). The conduction band of the nanocrystals consists of quantized energy sub-bands. The excitation of electrons in the conduction band from bound energy levels to continuum states will contribute in the generation of electrical current, as shown in Figure 1.2. [35] This type of photodetectors is called photoconductors. The conductivity of photoconductors increases upon illumination with sufficient energy, due to the generation of excess carriers. As a result, photoconductors can be used in detecting light, since they absorb photons and generate electrons.

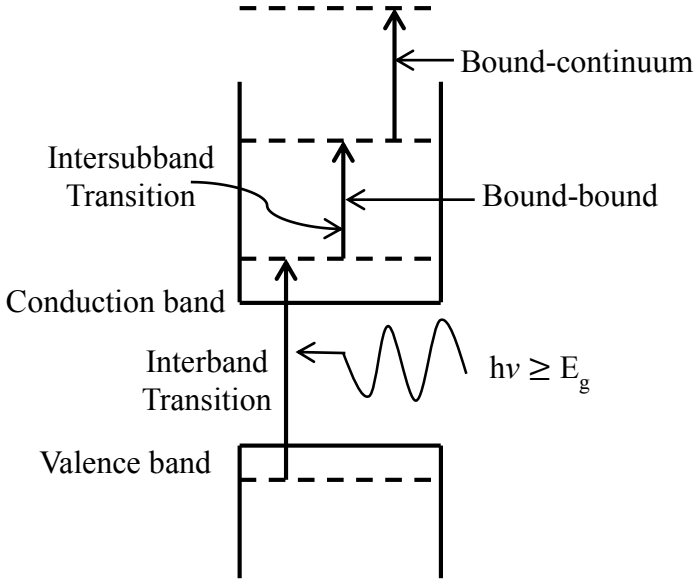

Figure 1.2 Schematic of interband transitions.

Photoconductors consist of single film of nanocrystals, and two metal contacts to provide electrical connections to the external circuit. Photoconductors require external bias voltage in order to collect the photo-excited carriers. Unlike photoconductors, photodiodes have junction and built-in electric field that helps in separating the photo-excited carriers without applying a bias voltage. Photoconductors offer photoconductive gain larger than unity, which can be defined as the number of circulated carriers per absorbed photons. Photoconductive gain is given by the ratio of the carrier life time to the carrier transit time.

Photoconductive gain can be increased by adding shallow trap states that capture one of the carriers while the other remains circulating. This will prolong the carrier life time since the recombination between carries is reduced. [36] High photocurrent (the current measured under photo-illumination) can be achieved by increasing the photoconductive gain. In ohmic system the photocurrent is given by the following equation:

$$J_{ph}=Gen\mu_n E \tag{1.2}$$

where J_{ph} is the photocurrent density, G is the photoconductive gain, e is the electron charge, n is the volume charge density, μ_n is the carrier mobility, and E is the applied electric field. The photocurrent is directly proportional to the photoconductive gain, as shown in equation 1.2.

The structure of photodiodes is more complicated compared to photoconductors. They require the formation of junction from two different semiconductors (heterojunction), same semiconductors (homojunction), or non-ohmic metal contacts (Schottky junctions). [36] Photodetectors that have metal-semiconductor-metal structure, can be fabricated using interdigitated electrodes. This structure consists of two back-to-back Schottky contacts. Furthermore, the height of the Schottky barrier junction is reduced after illumination, and therefore more carriers can cross the barriers giving rise to the photocurrent. [29]

Figures of Merit

Dark current is considered one of the important factors that are used to characterize the photodetectors. For high sensitivity applications, the dark current needs to be reduced to the minimum level, since it is considered as the source of noise. The sensitivity is defined as the minimum detectable amplitude of optical signal incident on the photodetector. [37] In other words, the photodetector needs to distinguish between the noise and optical signals. There are several sources of noise in photodetectors: Johnson noise (thermal), shot noise, and generation-recombination. Signal to noise ratio (SNR) is one of the figures of merits that are used to quantify the optical signal level. The signal level should be greater than the noise level in order to be detected. SNR is given by the following equation: [36]

$$SNR = \frac{RP}{i_n} \tag{1.3}$$

where R is the responsivity (A/W), P is the incident optical power (W), and i_n is the noise current.

Specific detectivity (D^*) is one of the common parameters that are used to characterize the performance of the detectors. It enables comparing photodetectors with different geometries in terms of the photoconductive material,[36] and it is calculated according to the following equation: [37]

$$D^* = \frac{R\sqrt{A}}{\sqrt{2eI_D}} \tag{1.4}$$

where A is the device active area, and I_D is the dark current. The unit of D^* is $cmHz^{1/2}W^{-1}$. In equation 1.4 the dominant source of noise is assumed to be shot noise that is caused by the flow of discrete charges. The detectivity is a function of different parameters, such as, the applied bias voltage, operation temperature, and incident wavelength.

C. POLARIZATION OF LIGHT

Unpolarized light is generated by electrons moving in random directions. Linear polarizer is used to produce a polarized light with single known polarization. In which only electric field parallel to the polarizer's transmission axes passes through. The mechanism of light polarization through liner polarizer is shown in figure 1.3 (a). As the light passes through the polarizer its intensity reduces according to Malus' law. The intensity of light transmitted through the polarizer is directly proportional to $\cos^2\theta$, where θ is shown in figure 1.3 (a) and defined as the angle between incident polarization and the transmission axis of the polarizer.

Wire grid polarizer is made from array of wires parallel to each other. Components of electric fields parallel to the wires are absorbed by converting them into waves propagating through the wires, and therefore their energy will be lost. On the other hand, electric fields

perpendicular to the wires are transmitted through the polarizer without losing their energy. [38] Figure 1.3 (b) shows the mechanism of light polarization through the wire grid polarizer, where E_v and E_h are the vertical and horizontal components of the electric field with respect to the wires, respectively.

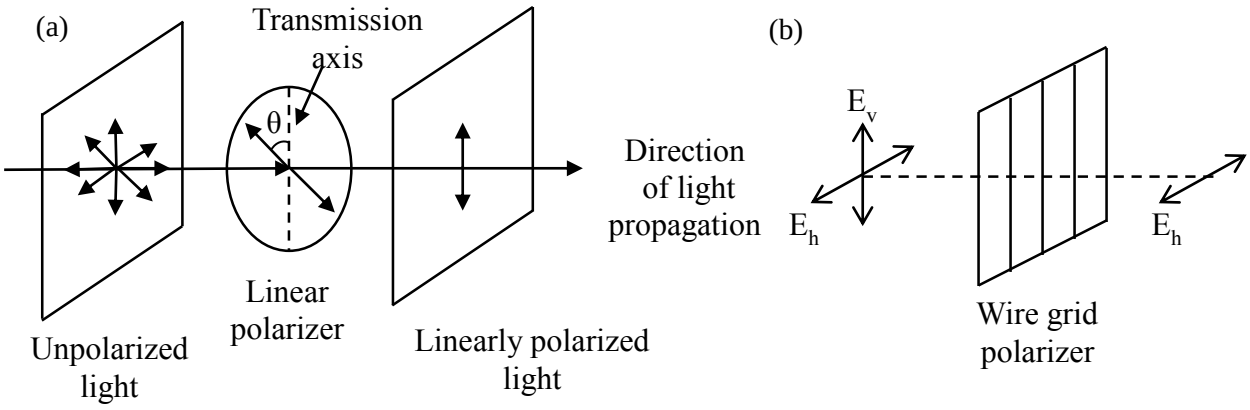

Figure 1.3 Mechanism of light polarization through: (a) linear polarizer (b) wire grid polarizer.

D. PLASMONIC EFFECT

Surface plasmons (SP) play a major rule in enhancing the optical near-field, they are collective charge density oscillations (electrons oscillating in synchronous) on metals surfaces coupled with incident light. The surface plasmons are considered as electromagnetic waves propagating along the interface between dielectric and metal, and decay evanescently in the direction perpendicular to the interface, as shown in figure 1.4. The interaction between the charge density fluctuations and the incident photons will result in great enhancement in the local optical field compared to the original incident radiations. [39]

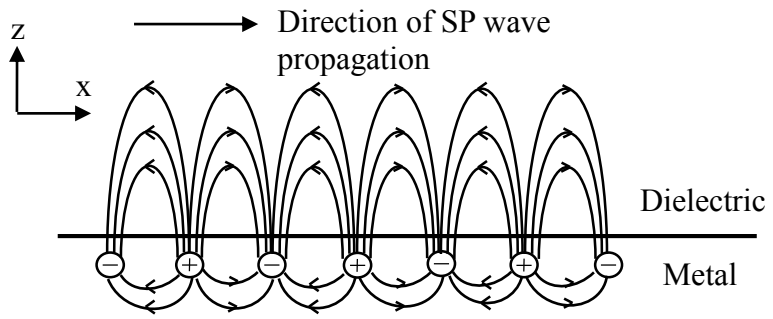

Figure 1.4 Surface charge oscillations at the interface between metal and dielectric material.

Plasmons were first observed by Wood in 1902. Another interesting form of plasmons present in the metallic particles called localized surface plasmons resonance (LSPR), which is responsible for the intense signals observed in surface-enhanced Raman scattering (SERS). [40] The SP wave can be described according to the following equation:

$$\vec{E} = \vec{E}\exp(-k_{zi}.|z|)\exp(-ik_{sp}.x - i\omega t) \tag{1.5}$$

where *i*=m (metal) for z<0 and *i*=d (dielectric) for z>0, k_{zi} is the wave vector along the z-axis, and k_{sp} is the wave vector of the SP wave and it given by the following equation:

$$k_{sp} = \frac{\omega}{c}\sqrt{\frac{\varepsilon_d \varepsilon_m}{\varepsilon_d + \varepsilon_m}} \tag{1.6}$$

where ω is the angular frequency, c is the speed of light, ε_d is the permittivity of the dielectric material, and ε_m is permittivity of metal. While the value of k_{zi} can be calculated from the wave equation ($d^2E(z)/dz^2 - k_{zi}^2E(z)=0$), and found to be $k_{zi}^2 = k_{sp}^2 - \varepsilon_i(\omega/c)^2$, where $\varepsilon_i = \varepsilon_d$ for z>0, and $\varepsilon_i=\varepsilon_m$ for z<0. From equation (1.6), the momentum of SP wave ($\hbar k_{sp}$) is larger than the momentum in free space ($\hbar k_o$, where $k_o = \omega/c$). Therefore, the surface plasmon wave is confined

to the interface, as it will decay if it propagates through both mediums (metal and dielectric). The mismatch in the wave vectors should be overcome in order to excite the SP waves. The wave vector of the incident photons can be increased by prism couplers or diffraction gratings.

Figure 1.5 is a plot of electric field given by equation 1.5 at the interface between free space (z>0) and gold (z<0). For this calculation the wavelength is 400 nm, and the corresponding permittivity of metal is -1.75. The decay of the electric field through the metal is higher than the decay through the dielectric, which is determined by the penetration depth.

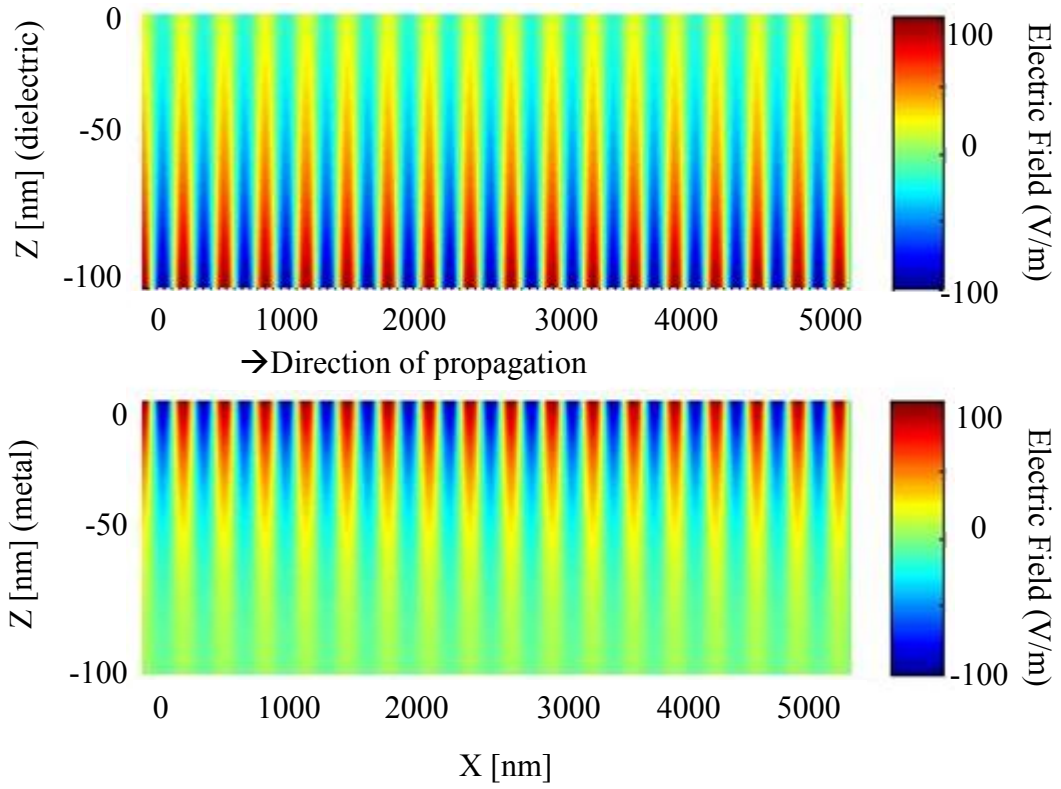

Figure 1.5 Plot of the electric field intensity for surface plasmon propagating along the interface (in the direction of x-axis) between free space (z>0) and gold (z<0).

II. MATERIAL GROWTH AND DEVICE FABRICATION

A. INTRODUCTION

In this project, semiconductor nanocrystals are synthesized and used in fabricating photodetectors. This chapter discusses the techniques of growing the nanocrystals and fabricating the devices. The nanocrystals were synthesized using wet chemical method, and the templates (interdigital metallization used to fabricate the devices) were prepared using standard optical photolithography. Section A will discuss the procedures to synthesize $CuInS_2$ and CdSe nanocrystals. While section B will deal with the preparation of the templates. Finally, section C will discuss the fabrication of the photodetectors.

B. SYNTHESIS OF NANOCRYSTALS

As mentioned previously the nanocrystals were synthesized using wet chemical method. This involves mixing the metals' precursors with an organic solvent in a three neck flask using magnetic stirrer bar. The synthesis was performed under the flow of N_2 gas. High temperature (>200 ^oC) was achieved using heating mantle, the setup of the synthesis is shown in figure 2.1.

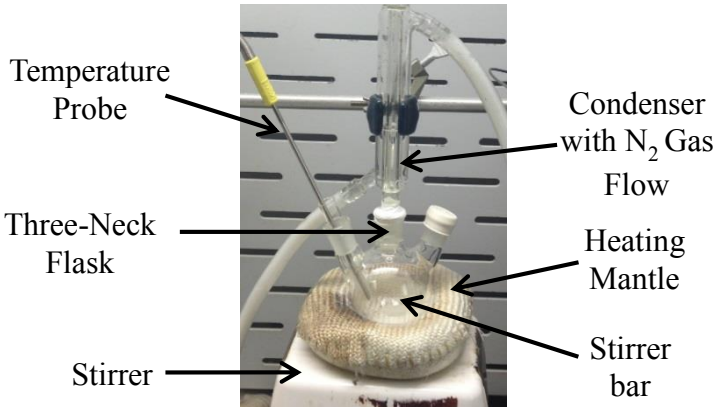

Figure 2.1 Synthesis setup, photo taken by the author in 6/1/2013.

$CuInS_2$ Nanocrystals

List of the chemicals used in the synthesis: copper(I) iodide (CuI), indium(III) acetates ($In(OAc)_3$) , 1-dodecanethiol (DDT), and 1-octadecene (ODE).

The nanocrystals were synthesized using one pot reaction, and according to previous reports with modifications, [41,42] which include the synthesis temperature, precursors amounts, and the reaction time. First, 1 mmol (190 mg) of copper(I) iodide and 1 mmol (292 mg) of indium(III) acetate are placed inside 50 ml three neck flask. Second, 5 ml of 1-dodecanethiol and 30 ml of 1-octadecene are added to Cu and In precursors. The thiols (DDT) are used as sulfur source and stabilizing ligands to control the reactivity of copper. Third, the three neck flask was placed under the fume hood while the middle neck is connected to the gas condenser. Then the flask was purged with nitrogen for 30 minutes to remove oxygen and other gases. The degasing step was performed by connecting the output of the condenser to a vacuum pump. This helped in speeding up the degasing process.

Afterwards, the mixture was vigorously stirred with a magnetic stirrer bar and preheated to 120 ^oC until a clear yellow solution was obtained. At this stage the solution is ready to start the nucleation by increasing the reaction temperature. Thus the mixture was heated rapidly to 230 ^oC within 3 minutes. This rapid increase in the temperature was achieved by using a heating mantle set at 230 ^oC, and wrapping fiber around the flask to maintain the heat and reduce the thermal loss to the surrounding atmosphere. When the nucleation starts the color of the solution gradually changes from yellow, to orange, to red, to brown, and finally it settles at dark brown, as shown in figure 2.2. The temperature of the reaction was maintained at 230 ^oC for 30 minutes. Finally, the reaction solution was quenched by cooling the flask in a water bath.

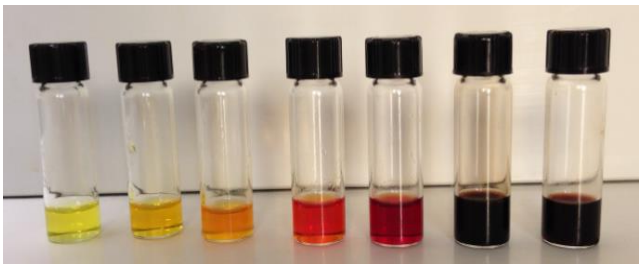

Reaction Time: Start 3 min 6 min 7 min 8 min 9.5 min 10.5 min

Figure 2.2 Color transitions of the reaction solution vs. reaction time, photo taken by the author in 6/1/2013.

In figure 2.3, the synthesis and purification procedures for $CuInS_2$ nanocrystals are summarized in a simple flow chart.

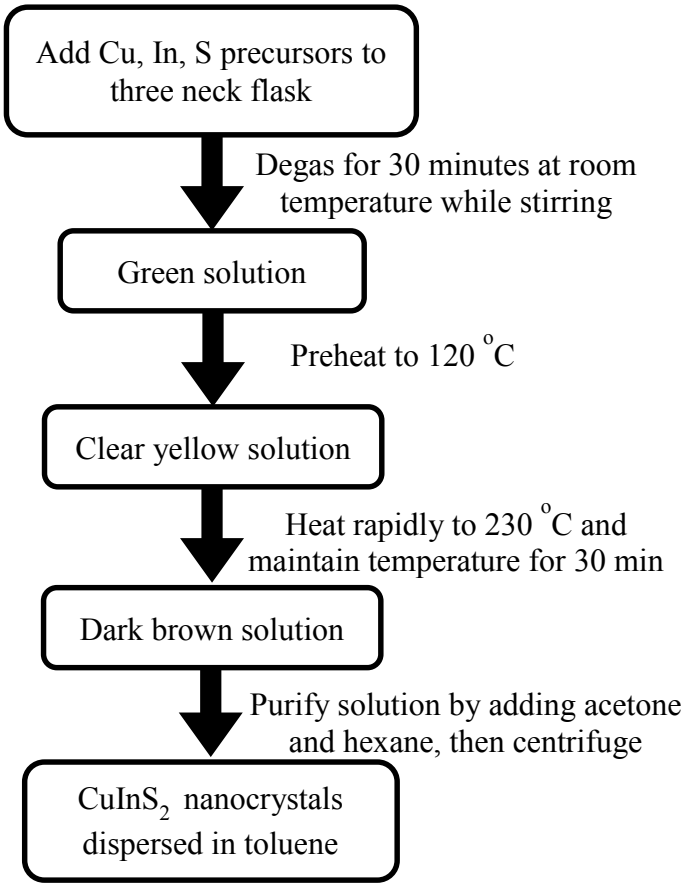

Figure 2.3 Flow chart of the synthesis and purification procedure for $CuInS_2$.

Following the synthesis process, purification of nanocrystals is important to remove the byproducts, such as, unreacted components, and excess thiols. This involves performing multiple cycles of precipitation on the dispersed nanocrystals. First, the nanocrystals in the original reaction solution are precipitated by adding excess acetone and centrifuging at 6000 rpm for 10 minutes. The supernatant (top part) was discarded and the precipitate containing the nanocrystals was collected and re-dispersed in 2 ml of hexane. Then the nanocystals were precipitated again by adding excess acetone and centrifuging. The addition of hexane is important to provide solubility for the nanocrystals, so the ligands between them will be protected from acetone. The process of precipitation and re-dispersion was repeated at least three times. The final product of purification process was collected and dispersed in hexane using ultra-sonication.

The contributions of this project was to find the optimal conditions for synthesizing high quality $CuInS_2$ nanocrystals applicable for fabricating optoelectronics devices. The previous reports on the synthesis of $CuInS_2$ nanocrystals hided lots of details related to the synthesis procedure. Rapid increase in the reaction temperature was one of the important steps for a successful synthesis, and helped in reducing the size distribution of the nanocrystals. Moreover, degasing step using vacuum pump was another contribution, which helped in removing oxygen and other gases. Another contribution for a successful synthesis, was preheating the mixture at temperature above 100 ^{o}C to ensure the evaporation of all the water contents from the reaction mixture. Finally, the use of hexane in the purification of nanocrystals was essential to prevent the nanocrystals from aggregation due the break of ligands, and to provide solubility for them.

CdSe Nanocrystals

List of chemicals used in the synthesis: cadmium oxide (CdO), elemental selenium (Se), 1-octadecence (ODE), n-trioctylphosphine (TOPO), and oleic acid.

The synthesis of CdSe nanocrystals was performed using hot injection method, and at high temperature according to previous reports with slight modifications, [43,44] which include the synthesis temperature, precursors amounts, and the reaction time. First, the selenium precursor was prepared by dissolving 4 mmol of selenium powder in 3 ml of n-trioctylphosphine at temperature of 60 ^{o}C for one hour. Second, the cadmium precursor was prepared by mixing 2 mmol of cadmium oxide with 1.5 ml of oleic acid and 7 ml of 1-octadecene at 100 ^{o}C in a separate 50 ml three neck flask using magnetic stirrer bar. Once the cadmium oxide was dissolved and became colorless, the selenium mixture was injected rapidly to the cadmium precursor at temperature of 270 ^{o}C. After that the nanocrystals were left to grow at 300 ^{o}C for one hour.

The synthesized CdSe nanocrystals were purified at least three times by following the same procedure adopted for $CuInS_2$ nanocrystals. But methanol was used instead of acetone and chloroform was used instead of hexane. In order to get rid of the long organic ligands, treatment with pyridine was performed for CdSe nanocrystals. [44] The nanocrystals were vigorously stirred in an excess of pyridine and under nitrogen gas atmosphere at temperature of 70 °C for 10 hours, then dried under vacuum overnight to remove excess solvents. Following the treatment with pyridine, the nanocrystals were finally dispersed in chloroform using ultra-sonication. Figure 2.4 summarizes the synthesis, purification, and treatment procedures of CdSe nanocrystals.

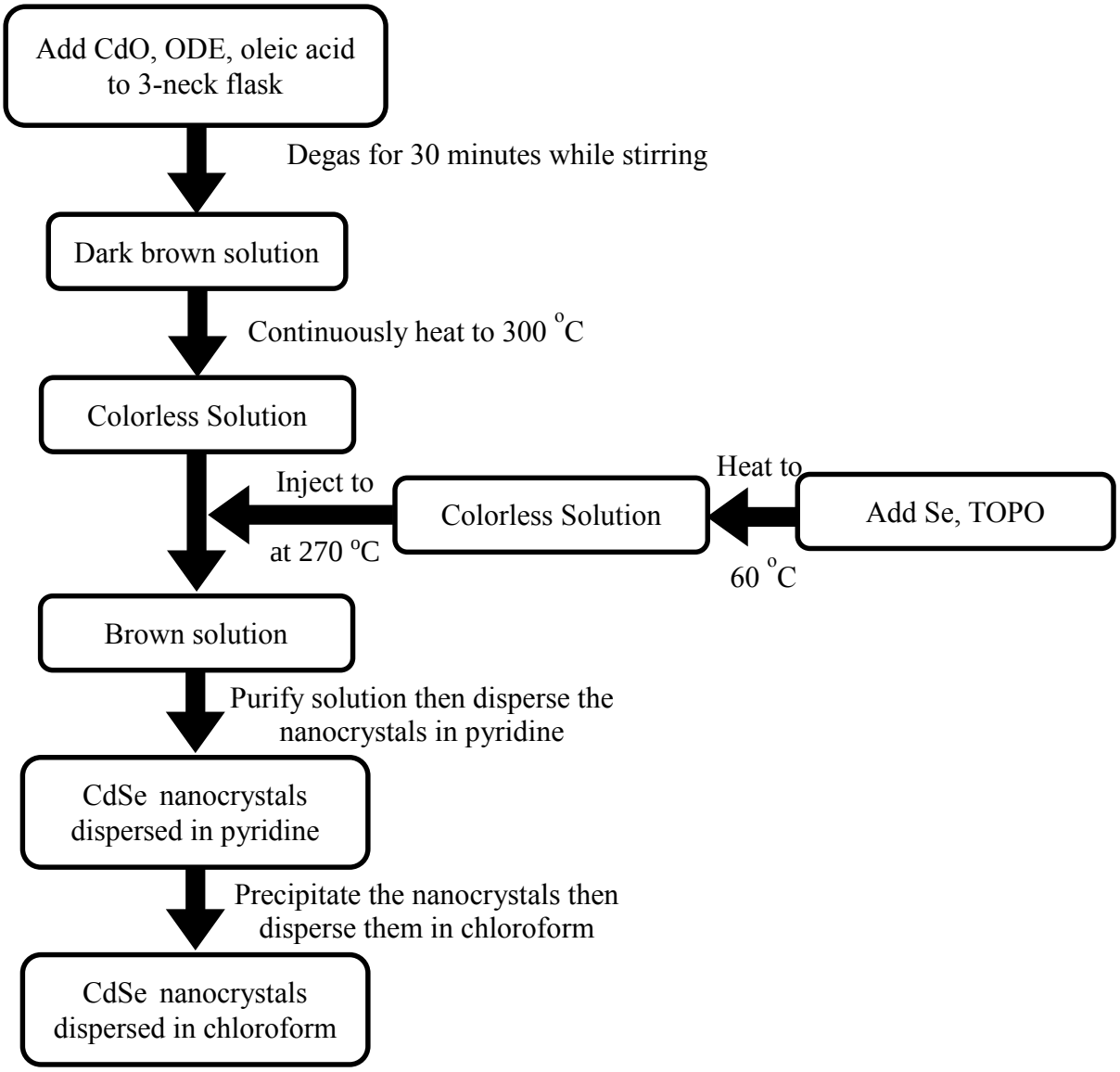

Figure 2.4 Flow chart of the synthesis, purification, and treatment for CdSe.

The project contribution was in performing the synthesis at high temperature (~300 °C) for one hour, which helped in creating large size of nanocrystals suitable for the photodetectors application. Also, the high reaction temperature helped in getting intense and narrow photoluminescence peak shifted to the near-infrared spectral region (730 nm).

C. PREPARATION OF TEMPLATES

The templates consist of interdigitated metallic electrodes deposited on glass substrates, with a channel that acts as a space between the two electrodes, as shown in figure 2.5. The electrodes were deposited on glass substrate to avoid short circuiting them. Templates with different electrode spacing (5, 10, 20, and 50 µm) were prepared. In the design of the templates, the aspect ratio between the channel width and the electrode width was 1:2. The nanocrystals will be deposited inside the channel, therefore the width of the channel will determine the characteristics of the fabricated device. The interdigital pattern helps in increasing the length of the channel without the need to increase the dimensions of the substrate. For example, the template with electrode spacing of 5 µm has a channel length of 600 mm, while the dimensions of the template are 3 x 7 mm. The total active area for the devices with electrode spacing of 5 and 50 µm are 0.03 and 0.05 cm^2, respectively.

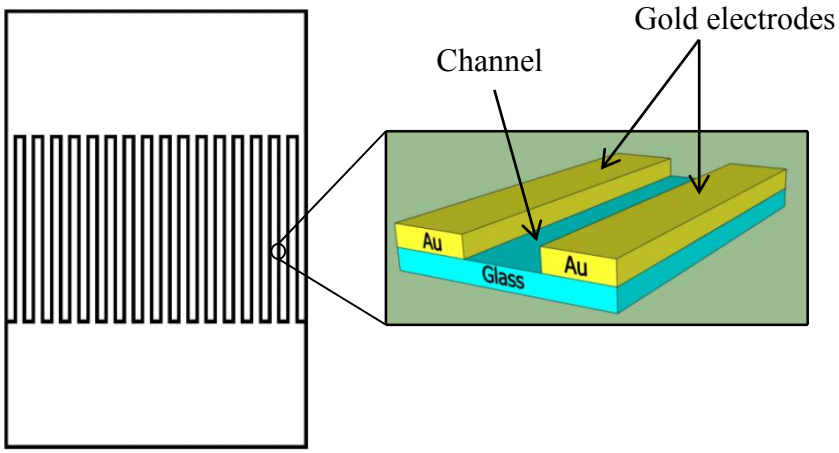

Figure 2.5 Sketch of the template with a magnified image of the channel.

The preparation of the templates was performed inside class 100 clean room using optical photolithography and according to the following steps:

Sample Cleaning

The glass substrate was cleaned by first soaking it in acetone for 3 minutes, then in methanol for 3 minutes. Next, the substrate was dried by blowing it with nitrogen, and cleaned with isopropanol and DI water. Finally, the glass substrate was dried by heating it at 150 ^{o}C for 5 minutes, to evaporate all the solvents' residuals that will affect the optical photolithography process.

Optical Photolithograph

Optical photolithograph was used to create perfect interdigital patterns with critical dimensions in micrometer range. This was achieved by designing a mask that has patterns with different dimensions, as shown in figure 2.6. The mask consists of dark lines of chrome deposited on a transparent glass substrate. Photolithography was performed using the following materials and equipment: positive photoresist (AZP 4330), developer (AZ 400K), spin coater, hot plate, and mask aligner with UV light source.

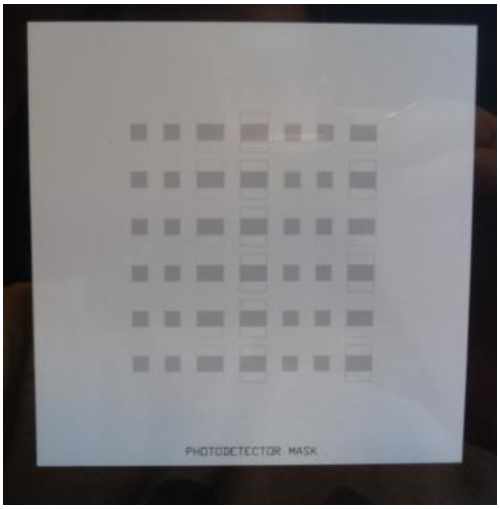

Figure 2.6 Image of the mask used in photolithograph, photo taken by the author in 6/1/2013.

First, the photoresist was deposited on the cleaned glass substrate using spin coating at speed of 7000 rpm for 1 minute. This will create a uniform film of photoresist with a thickness of 2.5 μm. Second, the photoresist film was baked at 110 ^{o}C for 3 minutes. Third, the sample was placed on the mask aligner, and exposed through the mask to UV light with intensity of 25 mW/cm^2. The exposed part of photoresist will be decomposed and can be removed by the developer. While part of the photoresist that falls below the dark lines of the mask will be protected from the light exposure. Fourth, the sample was developed in order to remove the exposed part of the photoresist. Finally, the sample was examined using microscope to ensure that the interdigital shape is perfect and does not have any breaks.

The exposer time is inversely proportional to the developing time, which means higher exposer time requires lower developing time. Also, the exposer time is directly proportional to the thickness of the photoresist film. The required exposer time for AZ 400K developer can be estimated by the following equation:

$$T = \frac{45 \times D}{I} \tag{2.1}$$

where T is the exposer time, D is the thickness of the photoresist (μm), and I is the intensity of the UV light (mW/cm^2). By using equation 2.1 the required exposer time is 4.5 seconds. The actual exposer time used in the experiments was 5 seconds. The optimal developing time was determined experimentally. The minimum developing time for a successful templates was found to be 25 seconds. Higher developing time is preferred since it will help in the lift-off process. However, excessive developing will destroy the patterns, since the developer starts attacking the unexposed portion of the photoresist. The previously mentioned procedure is summarized in figure 2.7.

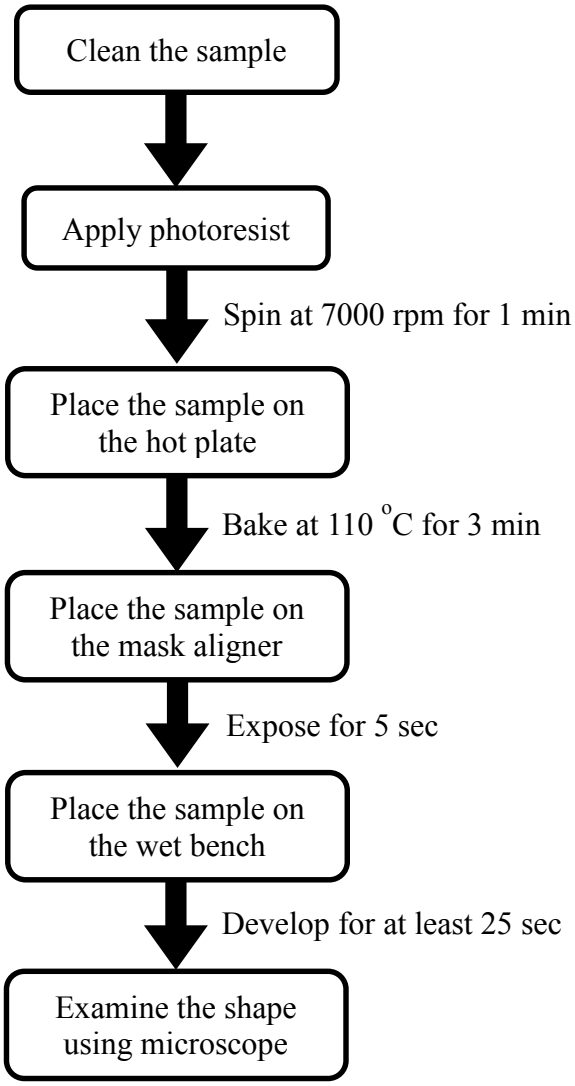

Figure 2.7 Flow chart summarizes the photolithography procedure.

Metallization

After the photoresist was exposed and developed, the samples were placed inside Nexdep e-beam evaporator. The metal was deposited under vacuum of 2×10^{-6} Torr and at room temperature. The deposited metals were Ti/Au. The titanium acts as an adhesive layer, since gold do not stick very well to the glass.

Lift-off

After the metal was deposited on the sample, the undeveloped portion of the photoresist was lifted using acetone. The sample was immersed in acetone and gently agitated either by a stream of acetone bubblies, or using ultra-sonication. After this process, the photoresist and the metal on top of it were removed, creating the channel and the interdigitated electrodes. The sample was examined using microscope to ensure that there are no residuals of photoresist. Open circuit test was performed on the electrodes using multi-meter, to ensure the electrodes are totally separated. Figure 2.8 shows images of the templates with different channel width after performing lift-off.

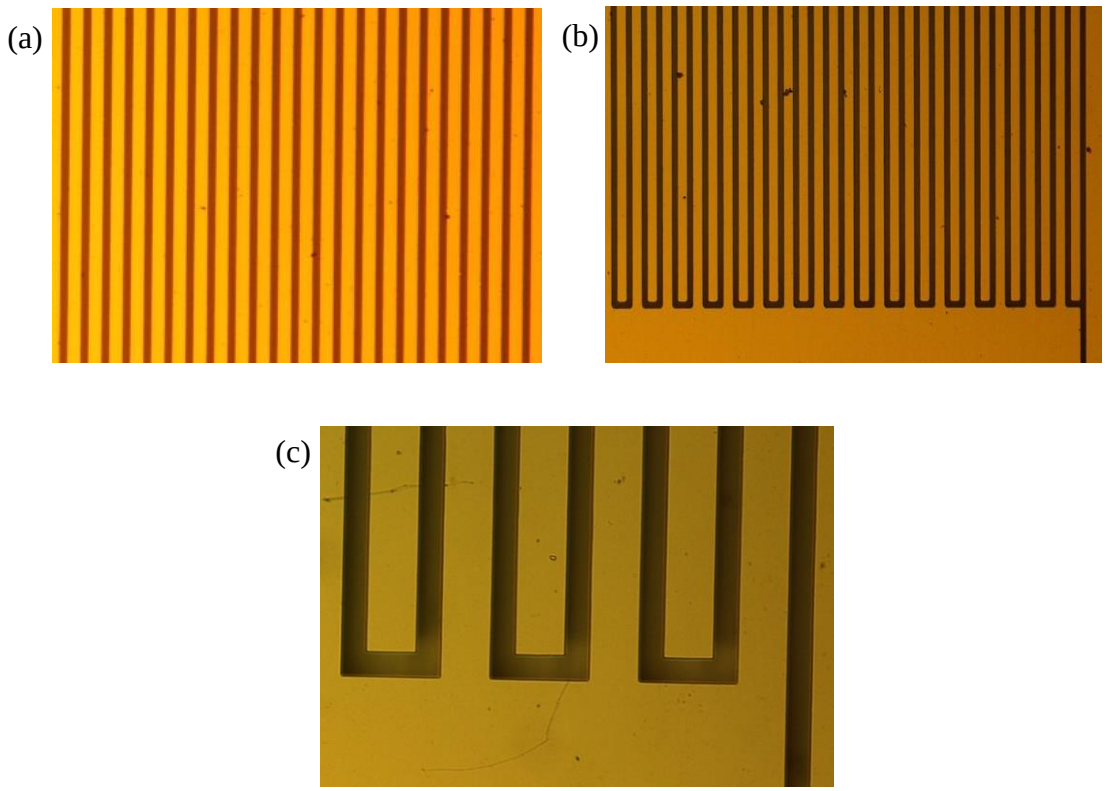

Figure 2.8 Image of the templates with channel width of (a) 5 µm (b) 10 µm (c) 50 µm

D. FABRICATION OF PHOTODETECTORS

The photodetector devices were fabricated by depositing the dispersed nanocrystals on the templates using spin coating. Following the deposition of the nanocrystals, the template was placed on a sampler holder that is made from copper plate and two gold plated connecters, as shown in figure 2.9. The electrodes of the template were coupled to the connecters of the sample holder using gold wire bonder.

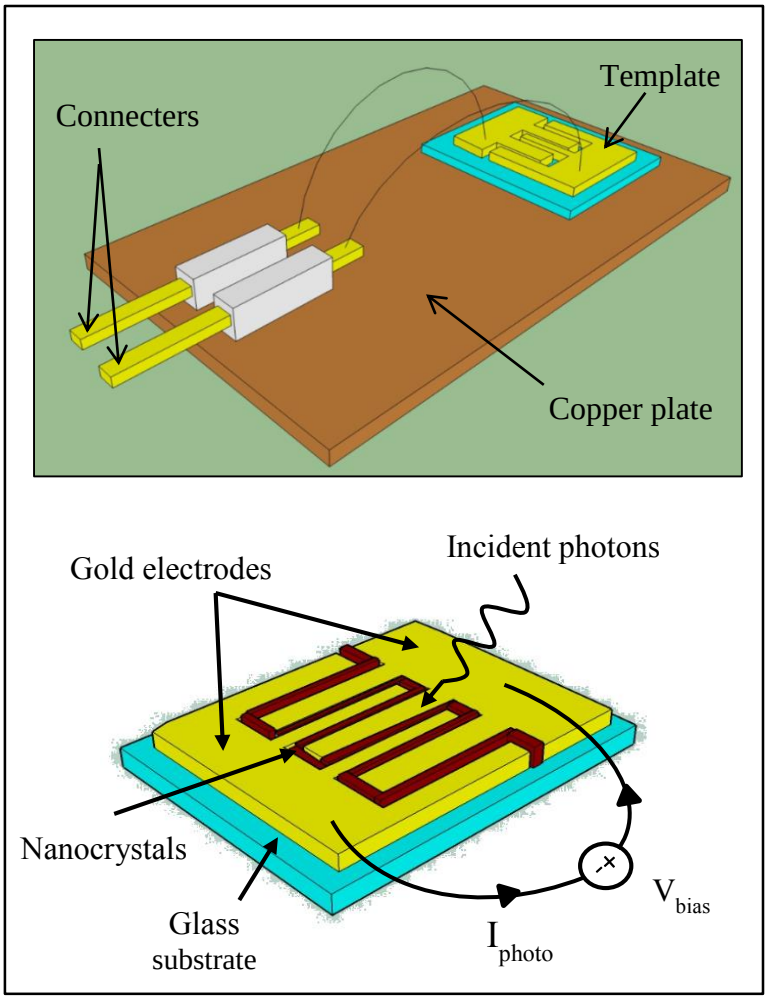

Figure 2.9 Sketches of the device.

III. CHARACTERIZATION TECHNIQUES

A. INTRODUCTION

This chapter will describe the characterization techniques used in the project. The material and device characterization techniques are divided into three main groups: optical, structural, and electrical. Section B will discuss the optical characterization techniques including: absorbance, photoluminescence, Raman scattering, and spectral response. While section C will discuss the structural characterization technique represented by x-ray diffraction. Finally, section D will discuss the electrical characterization technique.

B. OPTICAL CHARACTERIZATION

Optical Absorbance

The absorbance spectra of the nanocrystals in the ultra-violet, visible, and near-infrared spectral regions were measured using Cary 500 UV-Vis-NIR spectrophotometer. The wavelength scan of the spectrometer is in the range between 175 to 3300 nm. The nanocrystals were dispersed in a solvent, and placed inside quartz cuvette during the absorbance measurement.

As light travels through a medium, part of its energy is lost due to the absorbance or reflectance of the incident light. Absorbance can be expressed according to the following equation:

$$A = \log(\frac{1}{T}) = \log(\frac{I_o}{I}) \qquad (3.1)$$

where A is the absorbance, T is the transmittance, I is the transmitted light intensity, and I_o is the incident light intensity. In Carry 500 UV-VIS-NIR spectrophotometer the intensities of the incident and transmitted light are recorded at different wavelengths. When the energy of the incident photons is less than the bandgap of the nanocrystals, the photons are not absorbed and they are either reflected or transmitted. However, when the wavelength of the incident photons reduces their energy increases, once the energy becomes higher than the bandgap the photons are absorbed by the electrons. The excited electrons jump from the conduction band to the valence band (interband transition). The spectrophotometer uses double monochromator to produce single wavelength light (monochromatic light), and therefore the beam splitter is not needed.

Photoluminescence

Photoluminescence (PL) is a reversed process compared to the optical absorbance, and it involves the emission of photons as the excited electrons decay from the conduction band to the valence band. The PL spectra of the nanocrystals were measured by using a Horiba LabRAM spectrometer in conjunction with a 473 nm laser diode. The PL measurement was carried while the nanocrystals were placed on a glass slide and after the evaporation of the solvent (hexane/chloroform).

The laser was used as an excitation source. The emission from the nanocrystals, due to the decay of electrons from the conduction band to the valence band, is scattered back and detected by the spectroscopy. The PL intensity (arbitrary unit) was plotted against the wavelength (nm), and from the PL spectrum different information can be extracted like: the energy of band-to-band transitions, the size distribution of the nanocrystals, and the defects.

Raman Scattering

Semiconductor crystals consist of atoms that are bonded to each other. The quanta of the atom vibrations are called phonons, and they propagate through the crystal as waves. The traveling waves could be acoustical or optical. Two phonon modes exist depending on the direction of wave propagation with respect to the displacement, which is parallel in the longitudinal mode and perpendicular in the transverse mode.

There are two types of scattering: Rayleigh (elastic) and Raman (inelastic). Raman scattering is an inelastic scattering of light, which involves the excitation or absorption of vibrational modes. The shift between incident and scattered energies is called Raman shift. Usually Raman shift is expressed in terms of wavenumbers k ($k=2\pi/\lambda$) with a unit of cm^{-1}.

Raman shift has two types: Stokes or anti-Stokes. Let us assume that an incident laser beam with energy of $\hbar\omega_i$, where $\hbar$ is the reduced Plank's constant and ω_i is the incident angular frequency, was scattered by the crystal. If the scattered energy was $\hbar\omega_i + \hbar\omega$, then it is called Stokes shift. On the other hand, the scattered energy of anti-Stokes shift is $\hbar\omega_i - \hbar\omega$. On either case ω is independent ω_i, and it depends on the characteristics of the material.

Raman Scattering was measured using Horiba LabRAM spectrometer and under the excitation of laser beam. Optical filters are placed in the beam's path to pass the Raman scattered light to the spectroscopy and the detector, while blocking the transmittance of laser beam (Rayleigh scattering). Two types of filters were used: notch and edge. Figure 3.1 shows the optical configuration of the Raman spectroscopy. The laser beam excites the sample through optical microscope, and the Raman scattered light is collected and detected after filtration.

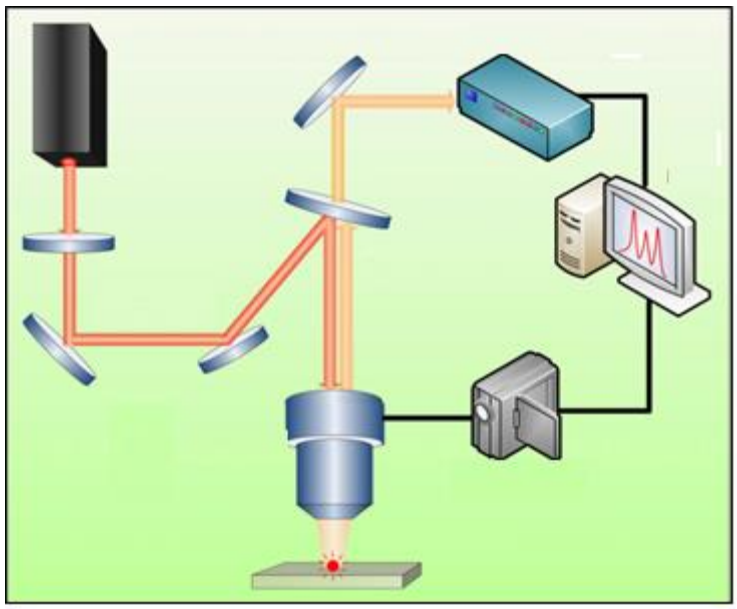

Figure 3.1 Sketch of Raman spectroscopy. [45]

Spectral Response

Spectral response is an optical characterization technique used to characterize the devices, and it is defined as the ratio of photo-generated current to the incident optical power. The spectral response intensity is expressed in arbitrary units and plotted versus the wavelength. The spectrum drops to zero at wavelengths above the bandgap of the nanocrystals. Since nanocrystals cannot absorb photons with energy lower than their bandgap. Therefore the device cannot generate current at energies lower than the bandgap.

In this project, the spectral response spectra were recorded using Bruker 125 HR Fourier transform infrared (FTIR) spectrometer in conjunction with Keithley 428 current preamplifier. FTIR spectroscopy is used to measure the absorbance or emission spectra. It is based on Michelson interferometer, which consists of a beam splitter, movable and fixed mirrors. The beam splitter splits the incoming beam into two separate beams, each traveling in a different

path. When the beams are reflected from the mirrors and recombined back on the beam splitter, inference occurs depending on the optical path difference. The total beam obtained from the recombination is detected by the detector (device to be tested). The output from the interferometer is called interferogram. As the position of the movable mirror varies the interferogram changes, and it is transformed into the spatial coordinate using Fourier transform. The position of the movable mirror is tracked using HeNe laser. The devices were placed inside Janis cryostat. Quartz halogen source was used as a broadband light source that covers the spectral range 400 - 2000 nm. Quartz beam splitter was also used in FTIR spectroscopy. The measurement was performed under vacuum of ~ 10^{-5} Torr. Figure 3.2 shows block diagram of FTIR spectroscopy.

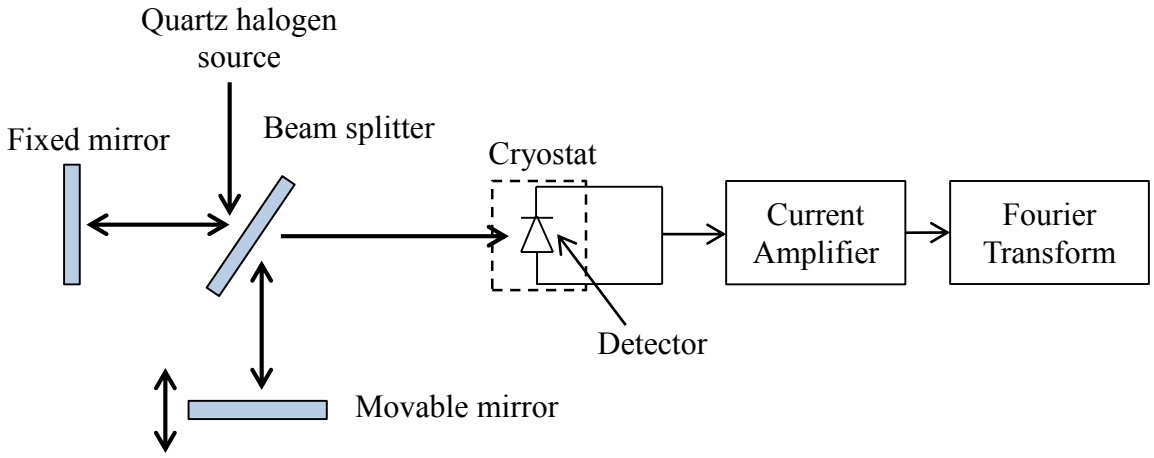

Figure 3.2 Block diagram of FTIR spectroscopy.

C. STRUCTURAL CHARACTERIZATION

The structural properties of CuInS2 nanocrystals were investigated using x-ray diffraction (XRD), which is a material characterization technique used to determine: the crystal structure, crystal orientation, and the lattice constant. In this measurement, x-ray beam strikes the layers of atoms within the crystal structure. Part of the x-ray beam is scattered and the other part passes through the layers of atoms, as shown in figure 3.3. The scattered x-ray beams interfere with each other and a diffraction pattern is created. When the scattered beams are in phase constructive interference is obtained, while out of phase scattered beams will interfere destructively.

According to Bragg's law, constructive interference between scattered beams occurs when the distance traveled through the layers of atoms is multiple of the wavelength of the beam. Diffraction patterns are plotted against the angle 2θ, where θ is shown in figure 3.3. The diffraction peaks (constructive interference) occurs at $\theta = \sin^{-1}(n\lambda / 2d)$, where *n* is an integer, λ is the wavelength of the beam, and *d* is the spacing between layers of atoms. The XRD measurement was performed using Philips PW 3040 X'PERT.

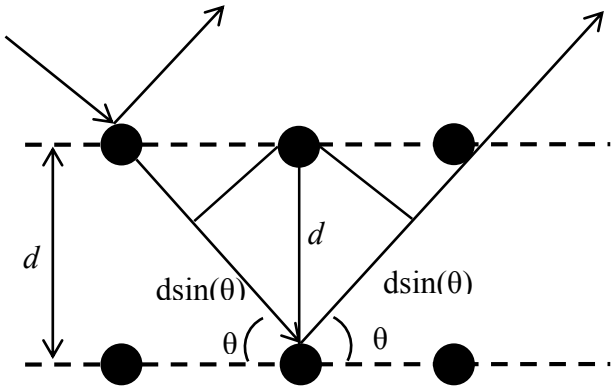

Figure 3.3 Scattering of x-ray beam.

D. ELECTRICAL CHARACTERIZATION

The current-voltage (I-V) characteristics of the photodetector were extracted using Keithley 4200 semiconductor parameter analyzer. The photocurrent was measured under the illumination of a broadband light source that covers the wavelength spectral range from 360 to 1800 nm, and with a power density of 350 mW/cm^2. The dark current was measured while the device was placed inside a dark chamber.

The I-V characterization system is made from source measuring unit that applies bias voltage and measures the current at the same time. The bias voltage is applied to the photodetector through one pair of high resistive measuring probes, while the current is measured through other separate pair of probes with lower resistivity. This configuration is called four probe measurement, and it decreases the error obtained in the measurement.

IV. RESULTS AND DISCUSSION

A. INTRODUCTION

In this chapter, the major characterization outcomes for both the materials and the devices are presented and discussed. Section B will discuss the characterization results of CdSe and $CuInS_2$ nanocrystals. Section C will discuss the results obtained from the CdSe photodetector. Finally, section D will discuss the current-voltage characteristics and spectral response spectra of semi-insulating GaAs photodetectors.

B. MATERIALS RESULTS

CdSe Nanocrystals

The synthesized CdSe nanocrystals were characterized by measuring the absorbance and photoluminescence spectra to determine the bandgap and the size distribution of them. Both spectra were plotted as function of the growth reaction time in figure 4.1 (a) and (b). [46] The absorbance spectra were measured for the nanocrystals while dispersed in chloroform and placed inside a cuvette. The PL spectra were measured for nanocrystals placed on a glass slide after evaporating the solvent (chloroform).

The growth reaction time was varied between 30 seconds and one hour. The absorbance and PL spectra showed a decrease in the bandgap of the nanocrystals as the reaction time increases. Which indicates that the size of the nanocrystals become larger with the reaction time. An increase in the growth reaction time beyond an hour does not produce nanocrystals with bandgaps lower than 1.7 eV (730 nm).

For an hour reaction time the PL spectrum consists of a single narrow peak positioned at 730 nm, indicating that the size variation of the nanocrystals is minimized. On the hand, the PL spectrum for 5 minutes reaction time consists of two peaks, which results from the presence of two dominant sizes for the nanocrystals. For shorter reaction times (< 3 min) the broad peak above 650 nm in the PL spectra is caused by unstable state in the nucleation stage. [43]

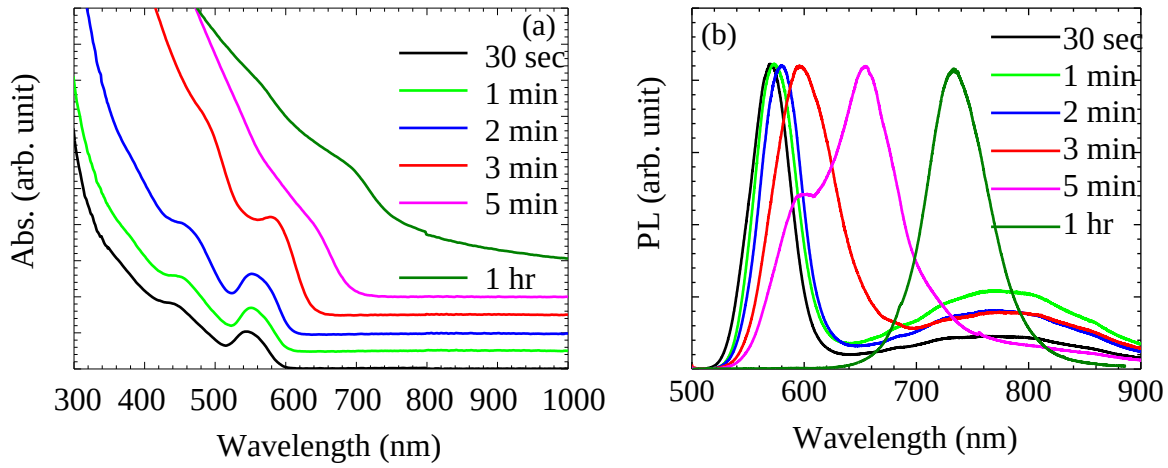

Figure 4.1 (a) Absorbance spectra of the dispersed CdSe nanocrystals grown at different reaction times are plotted against wavelength. (b) PL intensities are plotted versus wavelength at different reaction times. Reprinted with permission from Nusir *et al.* [46]

The peaks that appear in the absorbance spectra of the CdSe nanocrystals are called exciton absorption peaks, and they are caused by interband transition of electrons. Quantum confinement effect in the nanocrystals led to a discrete absorption spectrum, due to the transition of electrons between quantized energy states. The lowest two electron states in order of increasing in the energy are 1s and 1p. The first peak that occurs at lower energy of the absorption spectra is attributed to the transition of electrons from 1s state of the valence band to 1s state of the conduction band. While the second peak that occurs at higher energy of the absorption spectra is probably due to 1p-1p transitions.

$CuInS_2$ Nanocrystals

The optical properties of the synthesized $CuInS_2$ nanocrystals were extracted from the optical absorption and PL spectra of the dispersed nanocrystals. Figure 4.2 presents the absorption of nanocrystals grown at different growth reaction times. The reaction time was varied between 6 and 10.5 minutes. During the absorbance measurement, the nanocrystals were dispersed in toluene and placed inside quartz cuvette. The onset of the absorption spectra undergo a shift from 550 to 720 nm with increase in the reaction time. This indicates the growth of nanocrystals in a quantum confined system. The shoulder that appears in the absorption spectra is assigned to the excitonic transition in the nanocrystals.

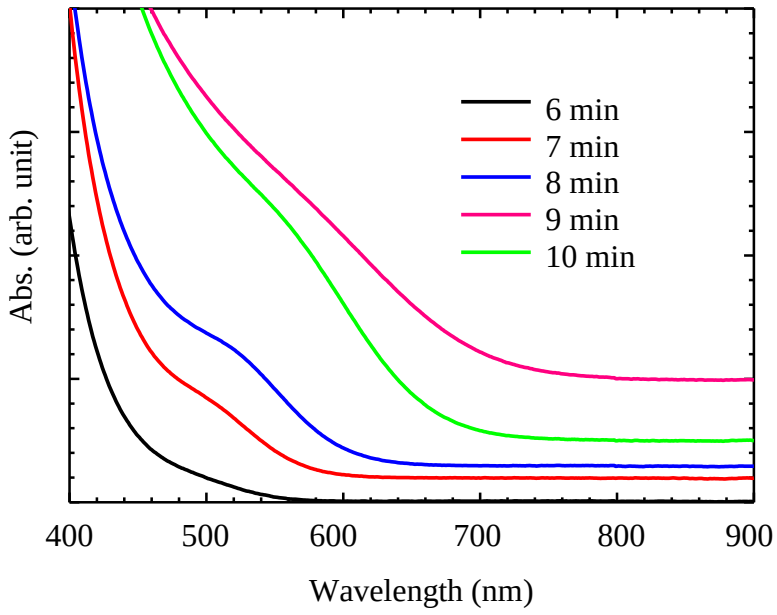

Figure 4.2 Absorption spectra of the $CuInS_2$ nanocrystals at different reaction times.

The PL spectrum of $CuInS_2$ nanocrystals grown at 230 ^oC for 30 minutes was measured and combined with the absorbance spectrum. As shown in figure 4.3, the PL spectrum of the nanocrystals consists of a single intense peak with narrow width positioned at 780 nm (1.59 eV). The slight shift between the PL peak and the absorbance threshold is attributed to Stokes Shift that results from electron-phonon interaction. As electrons decay from the conduction band to the valence band, they emit phonons. Therefore, the energy of emitted photons reduces, and the PL peak is shifted to a higher wavelength. The PL spectrum of the nanocrystals was measured at 77 K, to reduce the thermal excitation of electrons and to observe the excitons more clearly. The absorbance spectrum of the nanocrystals was measured at room temperature.

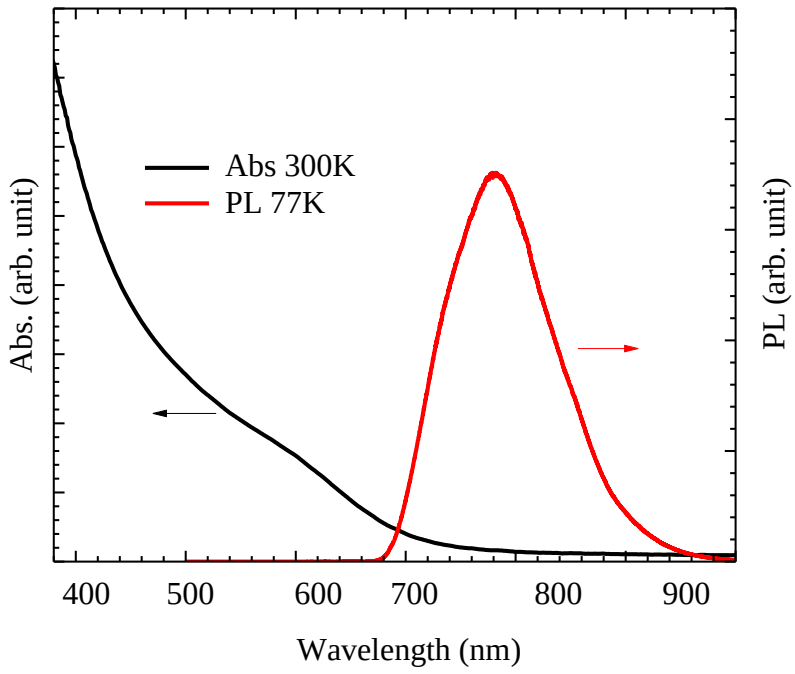

Figure 4.3 Absorbance and Photoluminescence spectra of $CuInS_2$ nanocrystals dispersed in toluene.

The crystalline phases of $CuInS_2$ nanocrystals were identified by measuring the Raman spectra of the nanocrystals. Normally, $CuInS_2$ nanocystals crystalline into chalcopyrite structure. Figure 4.4 represents the Raman spectra of two samples of $CuInS_2$ nanocrystals. The annealing condition for the sample was 110 ^oC for 30 minutes. The A_1 peak located at 300 cm^{-1} coincides with the literature, [47,48] and is assigned to the main vibrational mode associated with chalcopyrite phase.

The other peak observed at 340 cm^{-1} is assigned to E^1_{LO} vibrational mode and it also related to chalcopyrite phase. [47] No Raman peak was observed at 475 cm^{-1}, which indicates the absence of Cu_xS phases. [49] After annealing the nanocrystals, they become more crystalline and another peak appears at 305 cm^{-1} that is assigned to A_1* vibrational mode related to CuAu (non-chalcopyrite) phase. [49] This phase is derived from zincblende structure by re-ordering the cations (Cu^{+1}, In^{+3}), and it causes a decrease in the photovoltaic effect. [47]

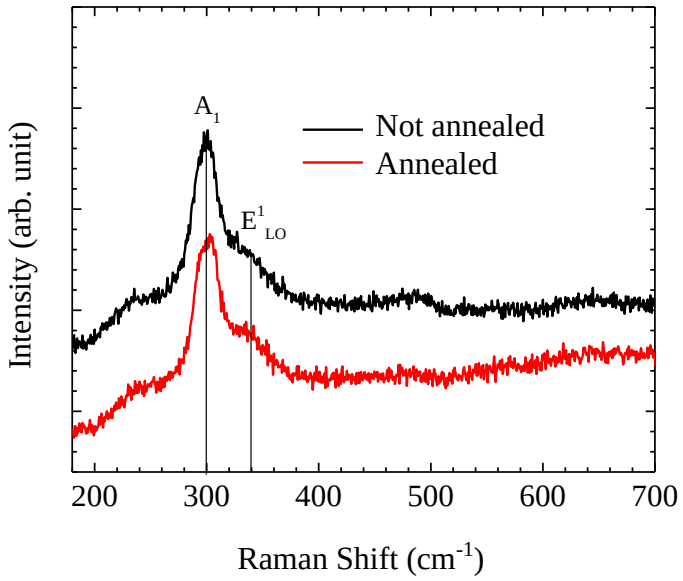

Figure 4.4 Raman spectra of $CuInS_2$ nanocrystals at different annealing conditions.

To study the structural dependence of $CuInS_2$ nanocrystals on the stoichiometric ratio, nanocrystals with different Cu:In ratio were synthesized and characterized. The Raman spectra of the synthesized nanocrystals are plotted in Figure 4.5. For 1:1 ratio the Raman spectrum consists of two peaks positioned at 290 and 340 cm^{-1}, and are related to chalcopyrite phase. Raman spectrum of copper poor samples showed the formation of CuAu structure, since the main peak is shifted to a higher wave number (309 cm^{-1}). This result matches with previous reports that showed Cu-deficient structures cause the formation of CuAu phase. [47] On the other hand, no CuAu phase is expected to form in copper rich samples, and the extra copper will form CuS segregation at the surface. [47]

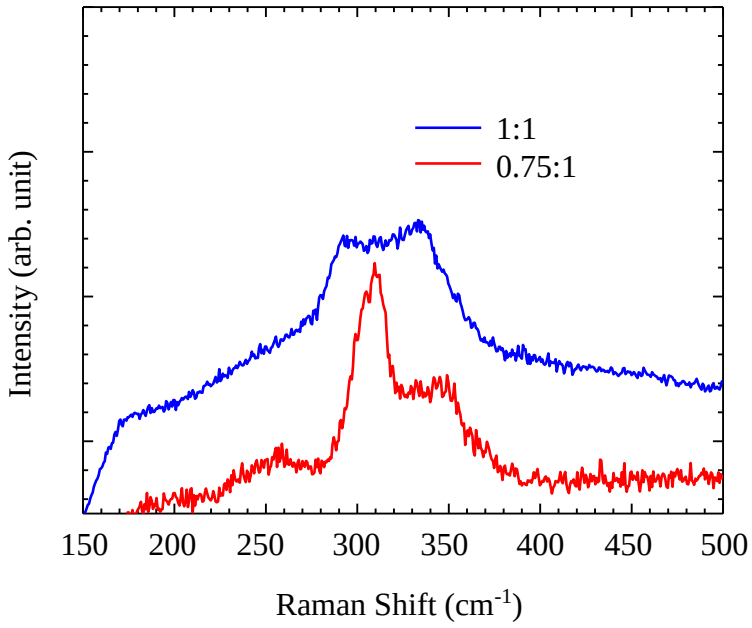

Figure 4.5 Raman spectra of $CuInS_2$ nanocrystals with different Cu:In ratio.

Structural characteristics of the synthesized $CuInS_2$ nanocrytals were investigated by means of x-ray diffraction (XRD). Figure 4.6 presents the XRD pattern of un-annealed sample. The diffraction peaks obtained at angles (2θ) of 28º, 48º, and 54º confirmed the formation of tetragonal crystal structure of $CuInS_2$ chalcopyrite. These peaks coincide with previous reports, [50,51] and in consistence with the respective "JCPDS" (Joint Committee on Powder Diffraction Standards) card No. 032-0339 for tetragonal $CuInS_2$. However, the strong peaks obtained at angles (2θ) of 34º, 37.6º, and 44º are attributed to the existence of copper oxide phase (CuO). Since these peaks are in consistence with JCDPS card No. 078-0428 for the cubic copper oxide.

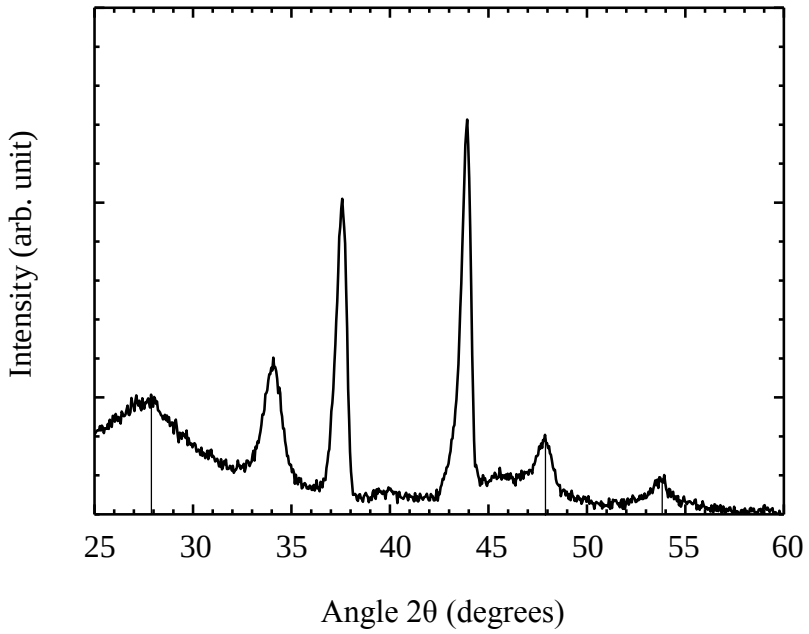

Figure 4.6 XRD pattern for $CuInS_2$ nanocrystals.

C. CdSe PHOTODETECTOR

I-V Characteristics

The current-voltage (I-V) characteristics for the CdSe photodetectors with electrode spacing of 1, 5, and 50 µm are plotted in figure 4.7. The dark current of the device with 50 µm electrode spacing was 0.25 nA at a bias voltage of 3 V (600 V/cm), whereas the photocurrent was 0.4 µA. By reducing the electrode spacing to 5 µm, the dark current was dropped to 28 pA and the photocurrent was increased to 3.8 µA at 3 V (6,000 V/cm) applied bias. As can be seen in figure 4.7, the photocurrent was about five orders of magnitude larger than the dark current.

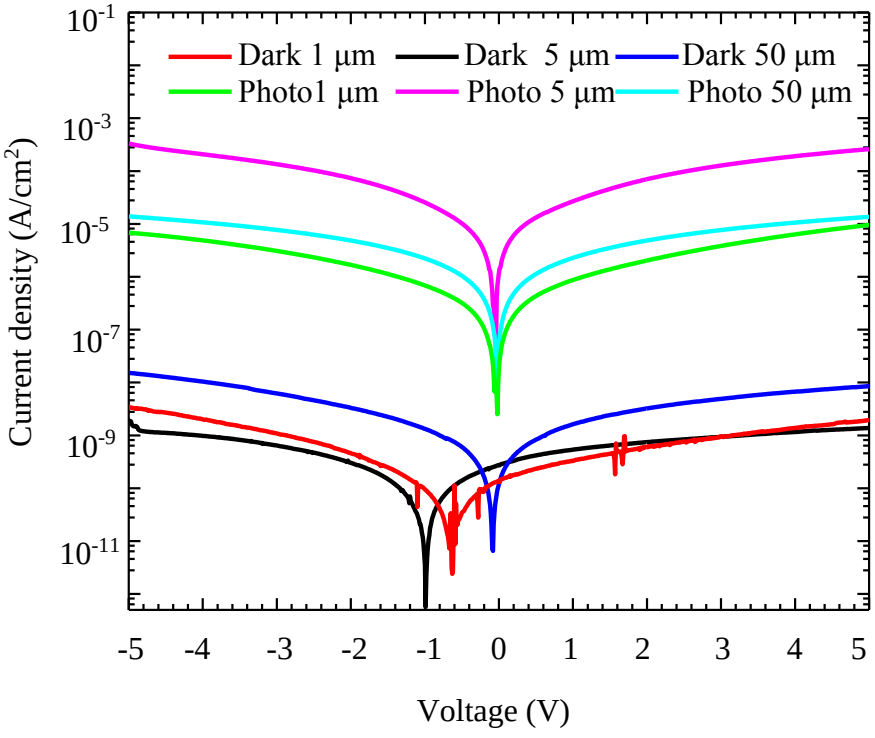

Figure 4.7 Current-voltage characteristics for devices with 1, 5, and 50 µm electrode spacing in dark and under illumination.

The I-V characteristics for the device with electrode spacing of 1 μm shows that dark current is 7.5 pA at bias voltage 3 V (30,000 V/cm), and the photocurrent to dark current ratio is three orders of magnitudes. The active area of the devices with electrode spacing of 1, 5, and 50 μm, are 0.008, 0.03, and 0.05 cm^2, respectively.

The device with its interdigital metallization structure creates a metal-semiconductor-metal interface, which consists of two back-to-back Schottky contacts. [52] When a bias voltage is applied, one Schottky contact is forward biased and the other is reverse biased. The open circuit voltage of the Schottky barrier junction becomes more pronounced with lower values of dark current as shown in figure 4.7 (a) for the 5 μm spacing device. The general expression for the open circuit voltage is given by the following equation: [53]

$$V_{OC} = \frac{E_g}{e} + \frac{nkT}{e}\ln\left(\frac{J_{sc}}{J_o}\right) \tag{4.1}$$

where V_{oc} is the open circuit voltage, E_g is the bandgap, n is the ideality factor, e is the electron charge, k is the Boltzmann constant, T is the absolute temperature, J_{sc} is the short circuit current density, and $J_o = A^*T^2\exp(-q\phi/KT)$ is the saturation current density, A^* is the Richardson constant (15.6 $A/cm^2.K^2$ for CdSe), and ϕ is the Schottky barrier height (0.68 eV). [54]

According to equation 4.1 the value of V_{oc} shifts to a negative quantity as the dark current is reduced, since the value of J_{sc} becomes very small compared with that of J_o which is around $4.2x10^{-5}$ A/cm^2. This also can be shown experimentally from figures 4.7, the 5 μm device has the lowest dark current density and the highest open circuit voltage. While the device with 1 μm spacing has higher dark current density and lower open circuit voltage compared to 5 μm spacing device. And finally the device with 50 μm spacing has the highest dark current density and the lowest open circuit voltage.

The detectivity of the photodetectors with 5 and 50 µm electrode spacing is plotted in figure 4.8 as a function of the applied bias voltage. [46] The detectivity of the devices at room temperature was extracted from the I-V curves and calculated using equation 1.4. High detectivity was obtained from the device with 5 µm electrode spacing, in which it was found to be 3.4×10^{10} $cmHz^{1/2}W^{-1}$ at 5 V (10,000 V/cm) applied bias voltage.

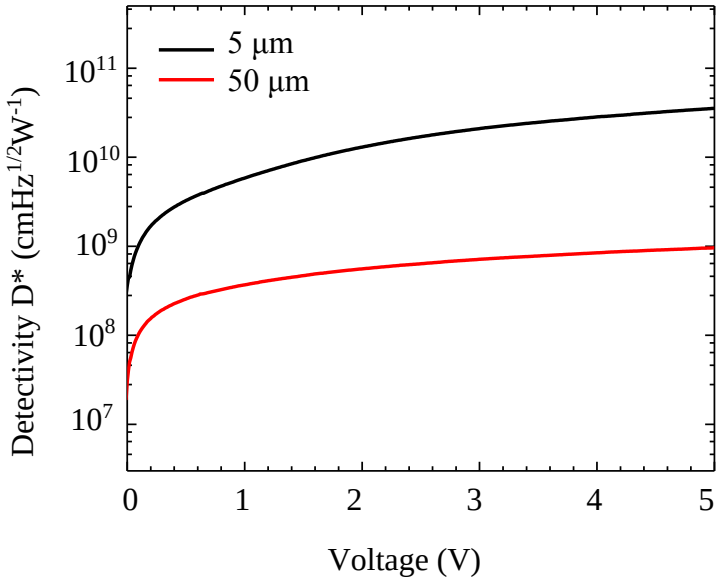

Figure 4.8 The detectivity of the photodetector was extracted from the I-V curve and plotted as function of the bias voltage. Reprinted with permission from Nusir *et al.* [46]

Spectral Response

The spectral response spectra were measured for the two devices at a bias voltage of 5 V and plotted in figure 4.9. [46] Higher spectral response intensity was obtained from the device with 5 µm electrode spacing compared with the 50 µm spacing device. The decrease in the electrode spacing shorten the transit time (t_r) of the carriers $t_r = d^2 / \mu V$, [55] where d is the electrode spacing, µ is the carrier mobility, and V is the applied bias voltage. Consequently, the

average carrier transit time affects the value of the photoconductive gain (G) as indicated by the following equation. [36]

$$G = \frac{\tau}{t_r} = \frac{\tau \mu V}{d^2}, \tag{4.2}$$

where τ is the carrier life time. According to equation 4.2 the photoconductive gain depends on the ratio of carrier life time to the carrier transit time. Therefore, the reduction in the electrode spacing is accompanied with increase in the spectral response intensity as shown in figure 4.9.

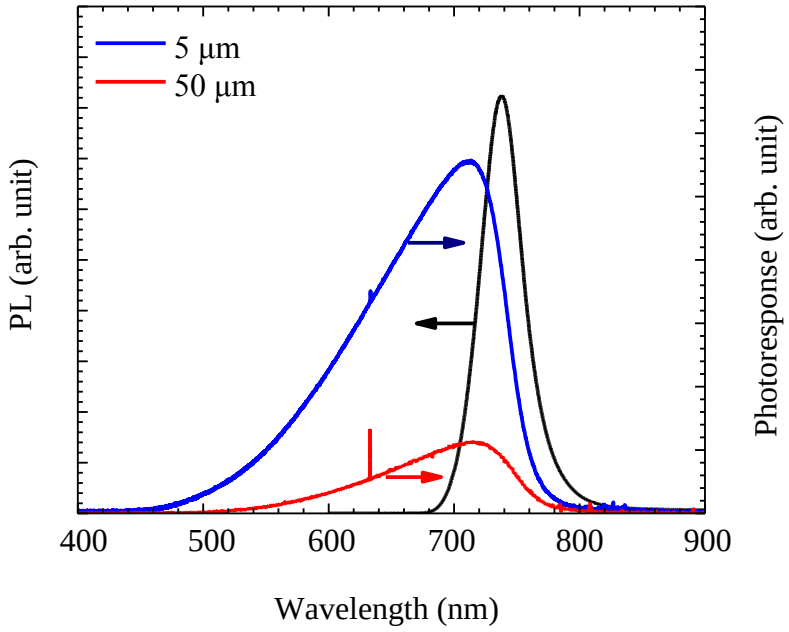

Figure 4.9 Spectral response and PL spectra were measured and plotted as a function of the wavelength. Reprinted with permission from Nusir *et al.* [46]

The spectral response of both devices has an onset at 710 nm wavelength. The rapid decay in the spectral response spectra below 700 nm is due to the response of the quartz beam splitter in the spectrometer. On the other hand, the absorbance spectra shown in figure 4.1 (a) do not exhibit a rapid decrease behavior similar to that observed in the photoresponse spectra. This

mainly because Carry 500 is a double monochromator and the beam splitter is not needed. The slight shift between PL spectrum of the nanocrystals and the device spectral response can be attributed to Stokes shift.

These results indicates that high detectivity was obtained in the visible-near-infrared spectral region compared with previous reports on CdSe photodetetors, [31,56] which exhibit a limited photocurrent to dark ratio within the visible region. The high detectivity observed here is perhaps due to the role of treatment with pyridine to remove the thick organic sheath surrounding the nanocrystals. These organic moieties affect the transfer of the carriers and act as recombination centers, which hamper the optoelectronic properties of the nanocrystals. [57]

D. SEMI-INSULATING GaAs PHOTODETECTOR

I-V Characteristics

The I-V characteristics of semi-insulating GaAs with interdigitated gold electrodes are presented in figure 4.10. The semi-insulating GaAs wafer has a resistivity of 2.2×10^8 Ω.cm, and carrier concentration of 5×10^6 cm^{-3}. Different electrode spacing (5, 10, 20, and 50 μm) were investigated. The photocurrent was measured under the illumination of boardband light source with intensity of 350 mW/cm^2. The dark current of the devices was on the order of 10^{-8} A, whereas the photocurrent was on the order of 10^{-2} A. The photocurrent to dark current ratio was around six orders of magnitudes, and increase with reduction in the electrode spacing of the device.

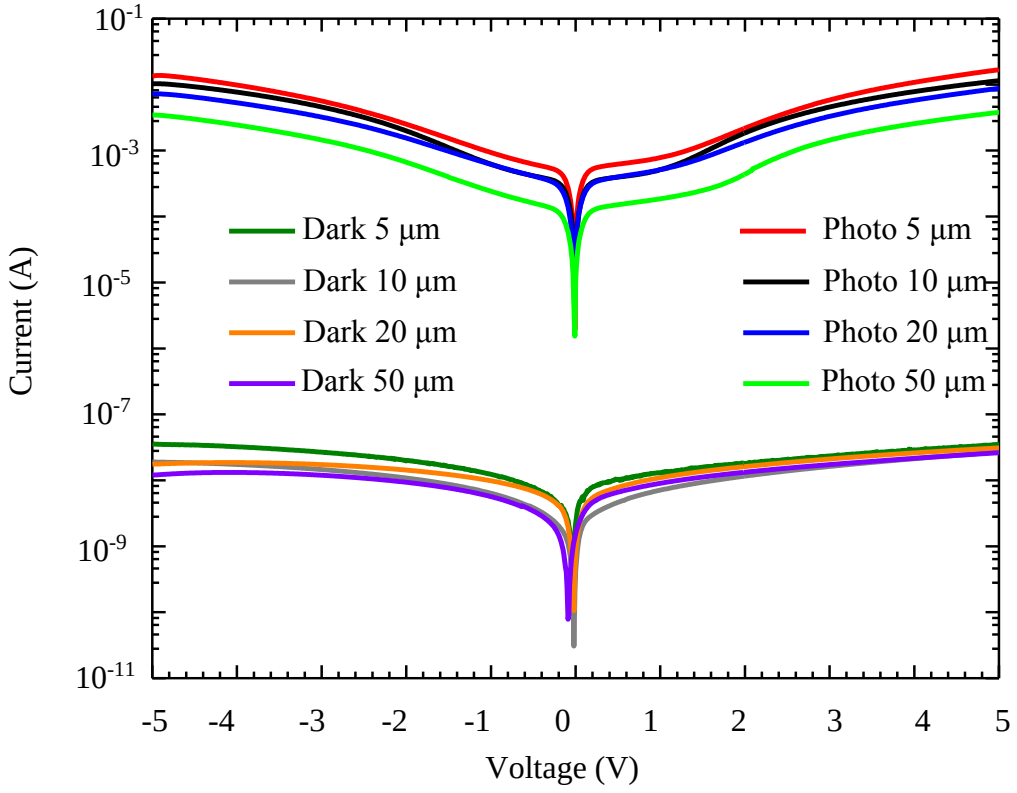

Figure 4.10 Current-voltage characteristics of devices on semi-insulating GaAs with different electrode spacing under dark conditions and photo-illumination.

The results obtained from the I-V curves showed an increase in the photocurrent as the electrode spacing decreases. This is mainly because the reduction in the electrode spacing is accompanied with increase in the carrier transit time, which increases the number of circulated carriers per absorbed photons. As a result, higher photoconductive gain can be achieved with lower electrode spacing. And higher photocurrent is also obtained, since it is directly proportional to the photoconductive gain as indicated by equation 1.2.

Spectral Response

Spectral response measurements were performed on the devices with different electrode spacing (5, 10, 20, and 50 μm) while biased at 1 V. No response was obtained for wavelengths above the bandgap of GaAs (870 nm), since the energy of incident photons is insufficient to excite electrons. As shown in figure 4.11, the highest spectral response was obtained from device with electrode space of 5 μm. The spectral response results were in consistence with the I-V curves and both showed an increase in the photocurrent as the electrode spacing was reduced. This results from the increase in the photoconductive gain with lower electrode spacing. The effect of interdigital shape on enhancing the response was investigated by fabricating a device with single gap of 2 mm wide. The spectral response of the 2 mm gap device was very weak compared with the others with interdigital metallization, as shown in figure 4.11.

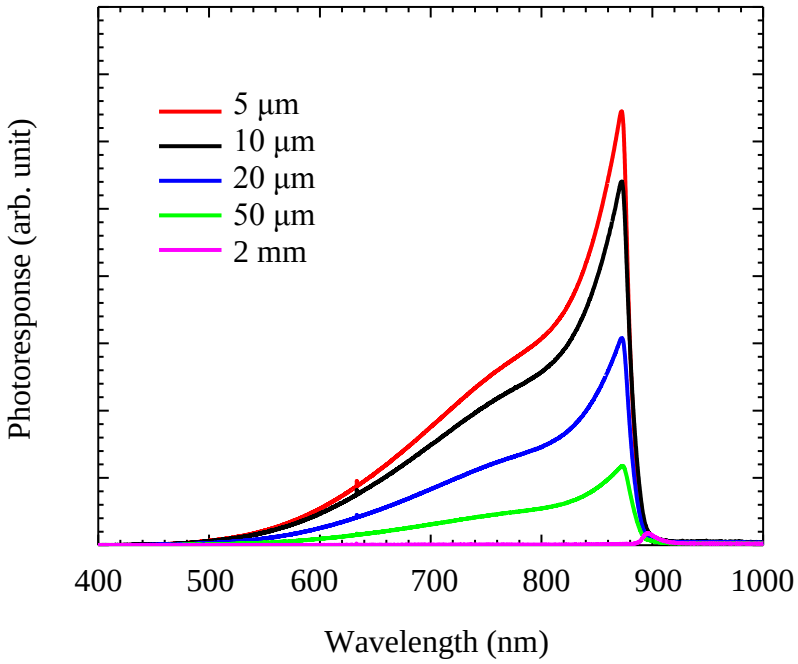

Figure 4.11 Spectral response of devices with different electrode spacing.

Polarizer Study

Significant enhancement in the spectral response was obtained as the spacing between electrodes was reduced from 50 to 5 μm. We believe that this enhancement is the result of high electric fields, and photon interaction with metal which may produce plasmonic effect. To confirm this assumption, polarizer study was performed on the devices to investigate the polarization dependence of the spectral response. The spectral response measurements were performed with two orientations of the polarizer's transmission axes: horizontal, and vertical. Also, the devices were tilted 90^{o} and the spectral response measurements were repeated.

Figure 4.12 (a) presents the spectral response of 5 μm spacing device with two orientations of the polarizer, while the electrodes of the device are in horizontal position. The intensity of the light drops after adding the polarizer, and therefore the spectral response of the devices were reduced too. The spectral response with vertically polarized light possesses higher intensity compared to the spectral response with horizontally polarized light.

Afterwards, the device was tilted 90^{o} with respect to the original position, in which the electrodes became in vertical position. The measurements were repeated again and the obtained spectra are plotted in figure 4.12 (b). For horizontally polarized light, the spectral response intensity was higher than that with vertically polarized light. However, the separation between the spectra in figure 4.12 (b) is reduced. Different variables may cause the reduction in the separation, especially that both experiments (before and after tilting the device) were not performed at the same time.

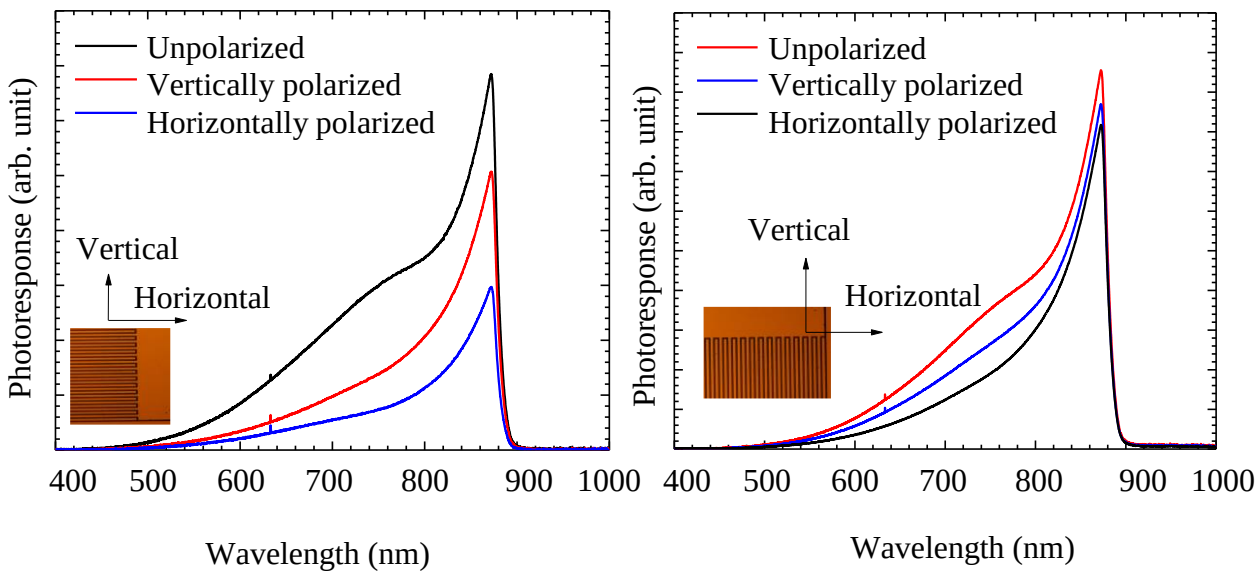

Figure 4.12 (a) Spectral response of the 5 μm device with two orientations of the polarizer. (b) Spectral response while the device is tilted 90°.

The previously mentioned procedure was repeated for device with electrode spacing of 10 μm, and the obtained spectral response spectra are plotted in figures 4.13 (a) and (b). First, the spectral response was measured while the electrodes of the device were in horizontal position. As shown in figure 4.13 (a), the spectral response with vertically polarized light exhibits higher intensity. Then the device was tilted 90° and the spectrum with horizontally polarized light was higher than that with vertically polarized light, as shown in figure 4.13 (b).

Polarization study was performed also on devices with electrode spacing of 20 and 50 μm, and the obtained spectral response spectra were plotted in figures 4.14 (a) and (b), respectively. Both measurements were carried while the electrodes of the devices were in horizontal position. No difference was observed in the spectral response of both devices as the polarization of the light was switched between vertical and horizontal positions, this can be seen in figure 4.14 (a) and (b).

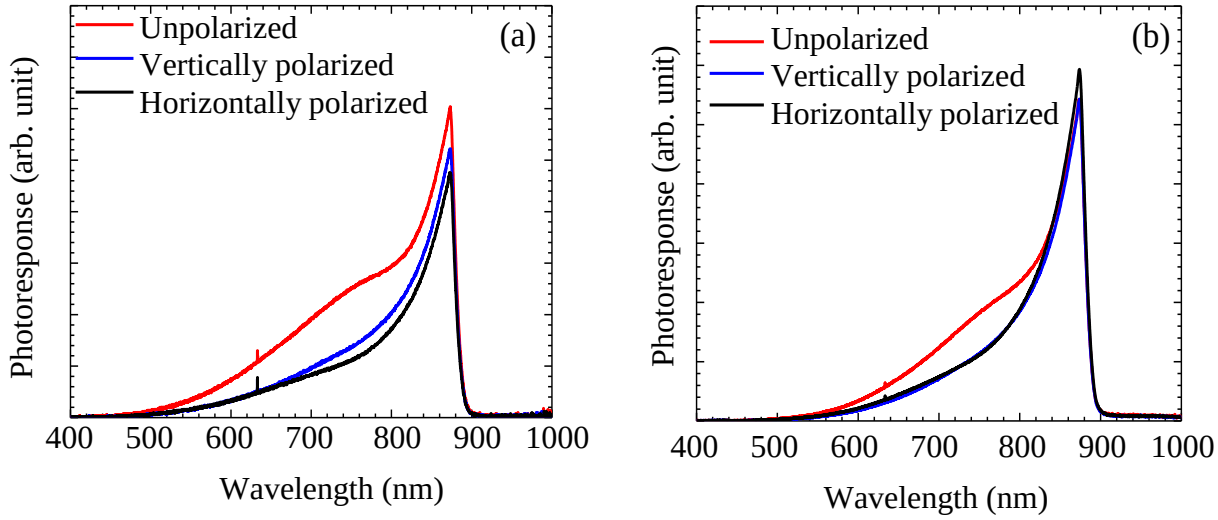

Figure 4.13 (a) Spectral response of the 10 μm device with two orientations of the polarizer. (b) Spectral response while the device is tilted 90°.

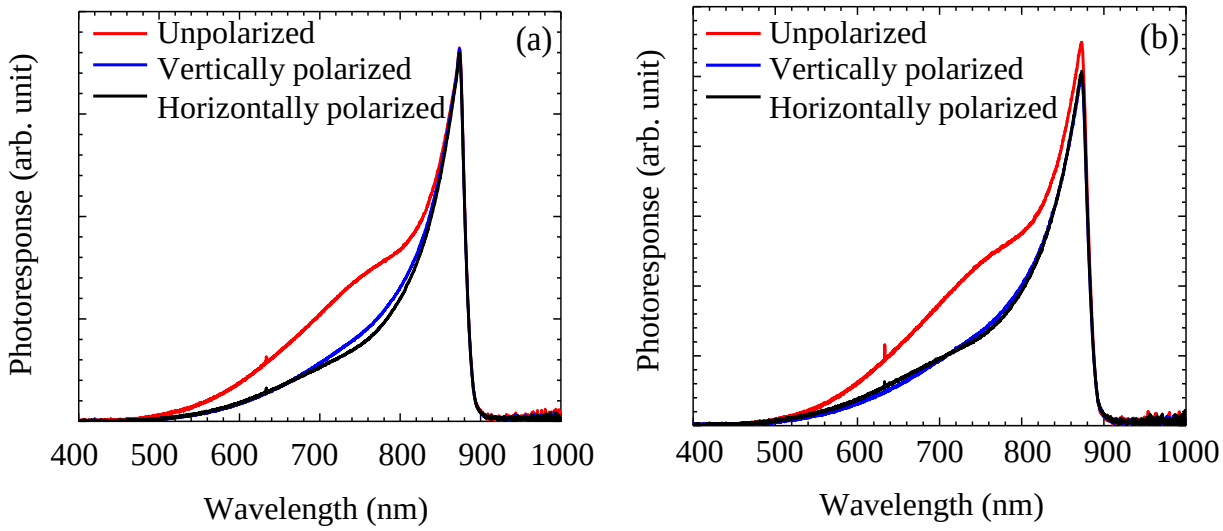

Figure 4.14 Spectral response of devices with spacing of (a) 20 μm (b) 50 μm.

As indicated from previous results, the spectral response was observed to be stronger for incident light with polarization across the interdigital electrodes (perpendicular to the electrodes), compared with light polarized along the electrodes (parallel to the electrodes). And the polarization dependence was observed to be highest in the device with electrode spacing of 5 and 10 μm. However, the spectral response spectra of devices with larger spacing (20 and 50 μm) did not show any polarization dependence.

According to the configuration of the electrodes, the circulation of the carriers is perpendicular to the electrodes. Therefore, enhancement in the electric field transverse to the electrodes will cause more carriers to circulate and will increase the photocurrent. On the other hand, longitudinal electric field will mainly be blocked by the electrodes and will not contribute in the enhancement of the spectral response. [38] This is similar to the mechanism of wire grid polarizer described in section C of chapter 1.

Figure 4.15 represents the distribution of surface plasmon (SP) waves inside gold electrode for a p-polarized incident light (the electric field is parallel to the plane of incidence xy). The x-axis represents the width of the electrode (10 μm) and the y-axis represents the thickness of the electrode (50 nm). As can be seen in figure 4.15, the SP wave propagates along the x-axis and decays in both directions (x and y). The SP wave can be described as following:

$$\vec{E}(x,y,z) = (E_x, E_y, 0)\exp(-k_y.|y|)\exp(-i(k_{sp}.x - \omega t) \qquad (4.3)$$

where k_{sp} is the wave vector of SP wave which is calculated using equation 1.6, and $k_y = \sqrt{k_{sp}^{\ 2} - \varepsilon_m k_o^{\ 2}}$, where ε_m is the permittivity of gold and k_o is the wave vector of free space.

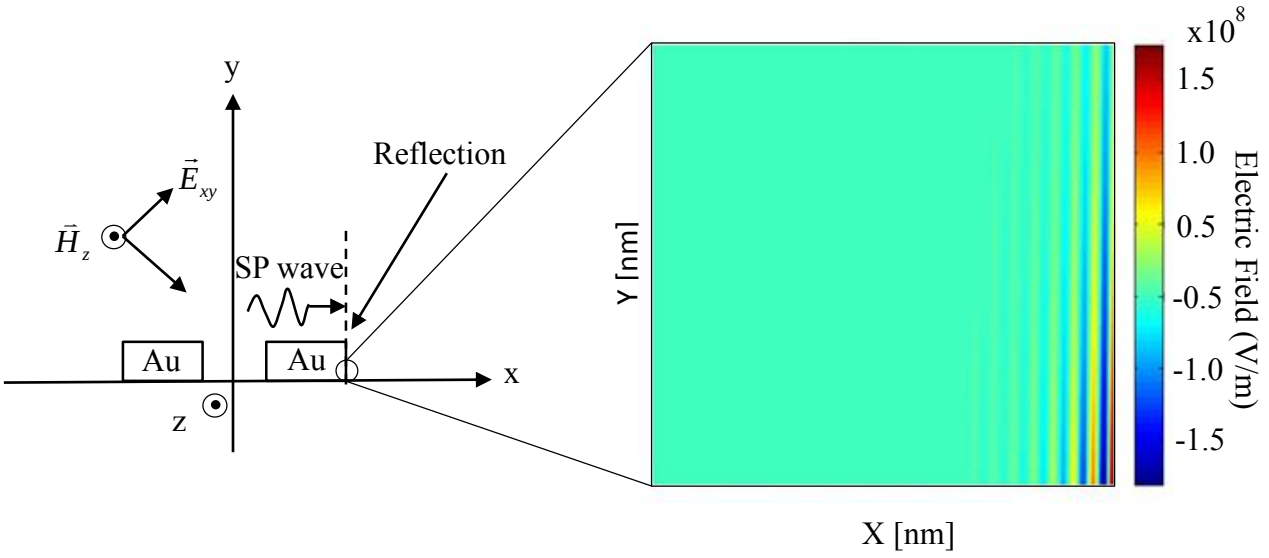

Figure 4.15 Cross sectional view of electric field inside the electrode for p-polarized wave.

The incident wavelength (λ_o) is equal to 440 nm, and the corresponding complex permittivity of gold at this frequency is equal to -1.75-5.4i. Since the permittivity of gold is a complex quantity, the value of k_{sp} is complex also. Therefore, the SP wave decays as it propagates along the x-axis. At x=*d* the SP wave will be reflected and there will be two waves propagating inside the metal: incident and reflected waves. The reflection coefficient (ρ) can be expressed according to the following equation:

$$\rho = \frac{n_m - n_d}{n_m + n_d} \tag{4.4}$$

where n_m and n_d are the refractive indices of the metal and the dielectric material, respectively. From figure 4.15, the SP wave is concentrated at the edge of the electrode.

For s-polarized incident light (electric field is perpendicular to the plane of incidence xy), the cross sectional view showing the distribution of the surface plasmon wave is plotted in figure 4.16. The SP wave propagates along the electrode and decays exponentially through the metal. The SP wave can be described according to the following equation:

$$\vec{E}(x,y,z) = (0,0,E_z)\exp(-k_y.|y|)\exp(-i(k_{sp}.z-\omega t) \tag{4.5}$$

As shown in figure 4.16, the electric field of the surface plasmon is concentrated at the surface of the electrode and decays in the direction of y-axis.

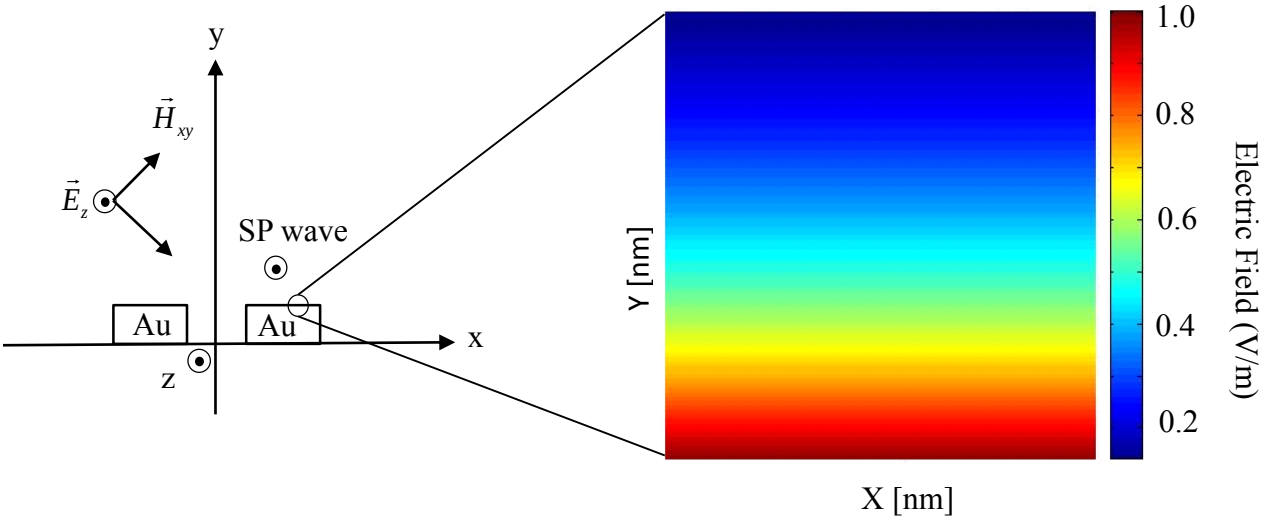

Figure 4.16 Cross sectional view of electric field inside the electrode for s-polarized wave.

From previous plots, we can conclude that the transvers polarized light creates a charge oscillation perpendicular to the electrode. And the resultant surface plasmon wave has high concentration at the edges of the electrodes. This will enhance the electric field between the electrodes. While in the case of longitudinal polarized light, the charge density oscillations are parallel to the electrode. And the excited surface plasmon wave will not contribute in the

enhancement of electric field between the electrodes, since the wave is concentrated at the surface of the electrodes. As the separation between electrodes increases, the electric field drops. Therefore, the enhancement in the electric fields due to the SP wave was not clearly observed in devices with larger electrode spacing (20 and 50 μm).

V. CONCLUSION AND FUTURE WORK

Conclusion

Two types of nanocrystals ($CuInS_2$ and CdSe) were investigated in this project. The nanocrystals were grown using wet chemical method, and characterized by: optical absorption and photoluminescence techniques. Several spectra were collected for nanocrystals grown at different synthesis time to show the growth of nanocrystals in a quantum confined system. The nanocrystals were purified and dispersed in a solvent for further processing. CdSe nanocrystals were functionalized by removing the long ligands to facilitate the transfer of carriers between the nanocrystals. The structural properties of $CuInS_2$ nanocrystals were investigated by measuring the Raman spectra and x-ray diffraction patterns.

Photodetectors based on CdSe nanocrystals were faricated by spin-coating the nanocrystals on interdigitated electrodes. The I-V characteristics and spectral response spectra were measured for two devices with electrode spacing of 5 and 50 μm. It was observed that the device with 5 μm spacing has a superior performance as compared to that with 50 μm spacing. The room temperature detectivity of the devices was extracted from the photocurrent and dark current and found to be on the order of $5x10^{10}$ $cmHz^{1/2}W^{-1}$ at bias voltage of 5 V.

Another photodetector was fabricated from semi-insulating GaAs and gold interdigitated electrodes. Enhancement in the spectral response was observed as the spacing between electrodes was reduced from 50 to 5 μm. Polarization study was performed on the devices, and showed that the spectral response depends on the polarization of incident light. Transvers polarized light with respect to the electrodes will produce transvers surface plasmon waves. These transverse plasmonic waves will enhance the electric field between the electrodes.

Future Work

Photodetectors based on CdSe nanocrystals have a spectral response at the edge of near-infrared spectral region (~710 nm), and it contains toxic and extremely dangerous heavy metals (Cd). Replacing these nanocrystals with cadmium free ones, such as $CuInS_2$, will produce environmental friendly devices, and can push the spectral response of the devices more into the near-infrared spectral region (~780 nm). Photodetectors based on $CuInS_2$ nanocrystals were not investigated yet, and it is considered as a promising technology in the field of optoelectronics devices for its distinctive optical and electrical properties.

The implementation of semi-insulating GaAs in light detection using interdigital metallization is considered encouraging. The high resistivity of the semi-insulating GaAs will provide low dark currents, and therefore high detectivity can be achieved at room temperature. Also, fabricating devices with smaller electrode spacing (< 1 μm) is expected to provide higher photocurrent to dark current ratio. The role of surface plasmon in the enhancement of the spectral response can be further investigated by plotting the electric field between the interdigitated electrodes using numerical solutions rather than analytical solutions.

REFERENCES

[1] S. K. Kailasa, K.-H. Cheng, and H.-F. Wu, "Semiconductor Nanomaterials-Based Fluorescence Spectroscopic and Matrix-Assisted Laser Desorption/Ionization (MALDI) Mass Spectrometric Approaches to Proteome Analysis**,"** *Materials*," vol. 6, pp. 5763-5795, 2013. doi.org/10.3390/ma6125763.

[2] R. S. Attaluri, S. Annamalai, K. T. Posani, A. Stintz, and S. Krishna, "Effects of Si doping on normal incidence InAs/In0.15Ga0.85As dots-in-well quantum dot infrared photodetectors," *J. Appl. Phys.* Vol. 99, pp. 083105-083107, 2006. dx.doi.org/10.1063/1.2189973

[3] L. E. Brus, "Electron–electron and electron-hole interactions in small semiconductor crystallites: The size dependence of the lowest excited electronic state," *J. Chem. Phys.* vol. 80, pp. 4403-4409, 1984. dx.doi.org/10.1063/1.447218

[4] A. P. Alivisatos, "Semiconductor Clusters, Nanocrystals, and Quantum Dots," *Science,* vol. 271,pp. 933-937, 1996. doi.org/ 10.1126/science.271.5251.933

[5] O. Manasreh, *Introduction to nanomaterials and devices*, New Jersey, USA: John Wiley & Sons Ltd., p. 201, 2012.

[6] R. Xie, U. Kolb, J. Li, T. Basche, and A. Mews, "Synthesis and Characterization of Highly Luminescent CdSe-Core CdS/Zn0.5Cd0.5S/ZnS Multishell Nanocrystals," *J. Am. Chem. Soc.* vol. 127, pp. 7480-7488, 2005. doi.org/10.1021/ja042939g.

[7] A. A. Guzelian, U. Banin, A. V. Kadavanich, X. Peng, and A. P. Alivisatos, "Colloidal chemical synthesis and characterization of InAs nanocrystal quantum dots," *Appl. Phys. Lett.* vol. 69, pp. 1432-1434, 1996. dx.doi.org/10.1063/1.117605.

[8] Y. Wang, A. Tang, K. Li, C. Yang, M. Wang, H. Ye, Y. Hou, and F. Teng, "Shape-controlled synthesis of PbS nanocrystals via a simple one-step process," *Langmuir*, vol. 28, pp 16436–16443, 2012. doi.org/10.1021/la303738u.

[9] F. M. Courtel, R. W. Paynter, B. Marsan, and M. Morin, "Synthesis, Characterization, and Growth Mechanism of n-Type $CuInS_2$ Colloidal Particles," *Chem. Mater.* vol. 21, pp. 3752–3762, 2009. doi.org/10.1021/cm900601k

[10] W. W. Yu , Y. A. Wang , and X. Peng, "Formation and Stability of Size-, Shape-, and Structure-Controlled CdTe Nanocrystals: Ligand Effects on Monomers and Nanocrystals," *Chem. Mater*. vol. 15, pp. 4300-4308, 2003. doi.org/10.1021/cm034729t

[11] M. Li, W. Zhou, J. Guo, Y. Zhou, Z. Hou, J. Jiao, Z. Zhou, Z. Du, and S. Wu, "Synthesis of Pure Metastable Wurtzite CZTS Nanocrystals by Facile One-Pot Method," *J. Phys. Chem. C*, vol. 116, pp. 26507-26516, 2012. dx.doi.org/10.1021/jp307346k

[12] M. Kruszynska, H. Borchert, J. Parisi, and J. Kolny-Olesiak, "Synthesis and Shape Control of $CuInS_2$ Nanoparticles," *J. Am. Chem. Soc.* vol. 132, pp. 15976–15986, 2010. doi.org/ 10.1021/ja103828f.

[13] D. H. Webber, and R. L. Brutchey, "Ligand Exchange on Colloidal CdSe Nanocrystals Using Thermally Labile *tert*-Butylthiol for Improved Photocurrent in Nanocrystal Films," *J. Am. Chem. Soc.* vol. 134, pp. 1085-1092,2012. dx.doi.org/10.1021/ja208878h.

[14] H. Zhong, Y. Zhou, M. Ye,Y. He, J. Ye, C. He, C. Yang, and Y. Li, "Controlled Synthesis and Optical Properties of Colloidal Ternary Chalcogenide $CuInS_2$ Nanocrystals," *Chem. Mater*. vol. 20, pp. 6434‑6443, 2008. doi.org/ 10.1021/cm8006827.

[15] V. J. Porter , Scott Geyer , J. E. Halpert , M. A. Kastner , and M. G. Bawendi, "Photoconduction in Annealed and Chemically Treated CdSe/ZnS Inorganic Nanocrystal Films." *J. Phys. Chem. C*. vol. 112, pp 2308-2316, 2008. doi.org/10.1021/jp710173q.

[16] D. V. Talapin, A. L. Rogach, A. Kornowski, M. Haase, H. Weller, "Highly Luminescent Monodisperse CdSe and CdSe/ZnS Nanocrystals Synthesized in Hexadecylamine−Trioctylphosphine Oxide−Trioctylphospine Mixture," *Nano Lett*. vol. 1, pp. 207-211, 2001. doi.org/10.1021/nl0155126.

[17] A. Kongkanand , K. Tvrdy , K. Takechi , M. Kuno , and P. V. Kamat, "Quantum Dot Solar Cells. Tuning Photoresponse through Size and Shape Control of CdSe−TiO_2 Architecture," *J. Am. Chem. Soc.* vol. 130, pp. 4007-4015, 2008. doi.org/10.1021/ja0782706.

[18] N. E. Coates, H. Zhou, S. Kramer, L. Li, and D. Moses, "Solution-Based In Situ Synthesis and Fabrication of Ultrasensitive CdSe Photoconductors," *Adv. Mater.* vol. 22, pp. 5366-5369, 2010. doi.org/10.1002/adma.201001150.

[19] J. Zhao, J. A. Bardecker, A. M. Munro, M. S. Liu, Y. Niu, I. Ding, J. Luo, B. Chen, A. K. Jen, and D. S. Ginger, "Efficient CdSe/CdS Quantum Dot Light-Emitting Diodes Using a Thermally Polymerized Hole Transport Layer," *Nano Lett.* vol. 6, pp. 463-467, 2006. doi.org/10.1021/nl052417e.

[20] S.-H. Wei, and S. B. Zhang, "Structure stability and carrier localization in Cd*X*(*X*=S,Se,Te) semiconductors," *Phys. Rev. B.* vol. 62 , pp. 6944-6947, 2000. doi.org/10.1103/PhysRevB.62.6944.

[21] A.-B. Chen, and A. Sher, *Semiconductor Alloys: Physics and Materials Engineering*, New York, USA: Plenum press, p.1, 1995.

[22] W. U. Huynh, J. J. Dittmer, and A. P. Alivisatos, "Hybrid Nanorod-Polymer Solar Cells," *Science*, vol. 295, pp. 2425-2427, 2002. doi.org/10.1126/science.1069156.

[23] M. Krunks, O. Bijakina, T. Varema, V. Mikli, E. Mellikov, "Structural and optical properties of sprayed $CuInS_2$ films," *Thin Solid Films*, vol. 338, pp. 125–130, 1999.

[24] C. Eberspacher, C. Fredric, K. Pauls, and J. Serra, "Thin-film CIS alloy PV materials fabricated using non-vacuum particles-based techniques," *Thin Solid Films*, vol. 387, pp.18-22, 2001.

[25] L. Li, N. Coates, and D. Moses, "Solution-Processed Inorganic Solar Cell Based on in Situ Synthesis and Film Deposition of $CuInS_2$ Nanocrystals," *J. Am. Chem. Soc.* vol. 132, pp. 22-23, 2010. doi.org/10.1021/ja908371f.

[26] M.-L. Lu, C.-W. Lai, H.-J. Pan, C.-T. Chen, P.-T. Chou, and Y.-F. Chen, "A Facile Integration of Zero- (I–III–VI Quantum Dots) and One- (Single SnO_2 Nanowire) Dimensional Nanomaterials: Fabrication of a Nanocomposite Photodetector with Ultrahigh Gain and Wide Spectral Response," *Nano. Lett.* vol. 13, pp. 1920-1927, 2013. dx.doi.org/10.1021/nl3041367.

[27] A. Luque, and S. Hegedus, *Handbook of photovoltaic and engineering*, United Kingdom: Wiley, p. 549, 2011.

[28] Y. Jin, J. Wang, B. Sun, J. C. Blakesley, and N. C. Greenham, "Solution-Processed Ultraviolet Photodetectors Based on Colloidal ZnO Nanoparticles," *Nano Lett.* vol. 8, pp. 1649-1653, 2008. doi.org/10.1021/nl0803702.

[29] H. Xue, X. Kong, Z. Liu, C. Liu, and J. Zhou, "TiO2 based metal-semiconductor-metal ultraviolet photodetectors," *Appl. Phys. Lett.* vol. 90, pp. 201118- 201118-3, 2007. doi.org/10.1063/1.2741128.

[30] G. Konstantatos, J. Clifford, L. Levina, and E. H. Sargen, "Sensitive solution-processed visible-wavelength photodetectors," *Nat. Photo.* vol. 1, pp. 531-534, 2007, doi.org/10.1038/nphoton.2007.147.

[31] D. C. Oertel, M. G. Bawendi, A. C. Arango, and V. Bulović, "Photodetectors based on treated CdSe quantum-dot films," *Appl. Phys. Lett.* vol. 87, pp. 213505-213505-3, 2005. doi.org/10.1063/1.2136227.

[32] B. S. Passmore, J. Wu, M. O. Manasreh, V. P. Kunets, P. M. Lytvyn, and G. J. Salamo, "Dual broadband photodetector based on interband and intersubband transitions in InAs quantum dots embedded in graded InGaAs quantum wells," *IEEE Electron Device Lett.* vol. 29, pp. 233508 - 233508-3, 2008. doi.org/10.1109/LED.2007.915371.

[33] Y. Bie, Z. Liao, H. Zhang, G. Li, Y. Ye, Y. Zhou, J. Xu, Z. Qin, L Dai, and D. Yu, "Self-Powered, Ultrafast, Visible-Blind UV Detection and Optical Logical Operation based on ZnO/GaN Nanoscale p-n Junctions," *Adv. Mater.* vol. 23, pp. 649-653, 2011. doi.org/10.1002/adma.201003156.

[34] R. Chang, and D. Perng, "Near-infrared photodetector with CuIn1-x AlxSe2 thin film**,"** *Appl. Phys. Lett.* vol. 99, 081103 - 081103-3, 2011. dx.doi.org/10.1063/ 1.3627185.

[35] A. Rogalski, J. Antoszewski and L. Faraone, "Third-generation infrared photodetector arrays," *J. Appl. Phys.*, vol. 105, pp. 091101 – 091101-45, 2009. dx.doi.org/10.1063/1.3099572.

[36] G. Konstantatos, and E. H. Sargent, "Solution-Processed Quantum Dot Photodetectors**,"** *Proceedings of the IEEE*, vol. 97, pp. 1666 – 1683, 2009. doi.org/10.1109/JPROC.2009.2025612.

[37] K.-J. Baeg, M. Binda, D. Natali, M. Caironi, and Y.-Y. Noh, "Organic Light Detectors: Photodiodes and Phototransistors," *Adv. Mater.* vol. 25, pp. 4267–4295, 2013. doi.org/10.1002/adma.201204979.

[38] X. J. Yu and H. S. Kwok, "Optical wire-grid polarizers at oblique angles of incidence," *J. of Appl. Phys.* vol. 93, pp. 4407-44013, 2003. doi.org/ 10.1063/1.1559937.

[39] J. Zhang, L. Zhang, and W. Xu, "Surface plasmon polaritons: physics and applications**,"** *J. Phys. D: Appl. Phys.* vol. 45**,** pp. 113001 (2012). doi.org/10.1088/0022-3727/45/11/113001.

[40] M. Rycenga, P. H. C. Camargo, W. Li, C. H. Moran, and Y. Xia, "Understanding the SERS Effects of Single Silver Nanoparticles and Their Dimers, One at a Time," *J. Phys. Chem. Lett.* vol.1, pp. 696-703, 2010. doi.org/10.1021/jz900286a.

[41] L. Li, T. J. Daou, I. Texier, T. Chi, N. Q. Liem, and P. Reiss, "Highly Luminescent $CuInS_2$/ZnS Core/Shell Nanocrystals: Cadmium-Free Quantum Dots for In Vivo Imaging," *Chem. Mater.* vol. 21, pp. 2422-2429, 2009. doi.org/10.1021/cm900103b.

[42] M. Booth, A. P. Brown, S. D. Evans, and K. Critchley, "Determining the Concentration of $CuInS_2$ Quantum Dots from the Size-Dependent Molar Extinction Coefficient," *Chem. Mater.* vol. 24, pp. 2064-2070, 2012. dx.doi.org/10.1021/cm300227b.

[43] H. Q. Nguyen, "Synthesis and optical properties of CdSe nanocrystals and CdSe/ZnS core/shell nanostructures in non-coordinating solvents," *Adv. Nat. Sci. Nanosci. Nanotechnol.* vol. 1, pp. 025004, 2010. doi.org/10.1088/2043-6254/1/2/025004.

[44] J. Park, K. H. Lee, J. F. Galloway, and P. C. Searson, "Synthesis of Cadmium Selenide Quantum Dots from a Non-Coordinating Solvent: Growth Kinetics and Particle Size Distribution," *J. Phys. Chem. C* vol.112**,** pp. 17849- 17854, 2008. doi.org/10.1021/jp803746b.

[45] Q. Tu, C. Chang, "Diagnostic applications of Raman spectroscopy," *Nanomed.* vol. 8, pp. 545–558, 2012. doi.org/10.1016/j.nano.2011.09.013.

[46] A. I. Nusir, J. Aguilar, Z. Bever and M. O. Manasreh, "Uncooled photodetectors based on CdSe nanocrystals with interdigital metallization," Appl. Phys. Lett. vol. 104, pp. 051124-051128, 2014.dx.doi.org/10.1063/1.4864636.

[47] T. Riedle, "Raman Spectroscopy for the Analysis of the Thin CuInS2 Films," Ph.D. Thesis, Technical University of Berlin, Berlin, Germany, 2002.

[48] F. M. Courtel, R. W. Paynter, B. Marsan, and M. Morin, "Synthesis, Characterization, and Growth Mechanism of n-Type $CuInS_2$ Colloidal Particles," *Chem. Mater.* vol 21, pp. 3752–3762, 2009. doi.org/10.1021/cm900601k.

[49] J. Alvarez-Garcia, "Characterisation of CuInS2 films for solar cellapplications by Raman Spectroscopy," Ph.D. Thesis, University of Barcelona, Barcelona, Spain, 2002

[50] S. L. Castro, S. G. Bailey, R. P. Raffaelle, K. K. Banger, and A. F. Hepp, "Synthesis and Characterization of Colloidal CuInS2 Nanoparticles from a Molecular Single-Source Precursor ," *J. Phys. Chem. B.* vol. 108, pp. 12429-12435, 2004. doi.org/10.1021/jp049107p.

[51] M. G. Panthani, V. Akhavan, B. Goodfellow, J. P. Schmidtke, L. Dunn, A. Dodabalapur, P. F. Barbara, and B. A. Korgel, "Synthesis of $CuInS_2$, $CuInSe_2$, and $Cu(In_xGa_{1-x})Se_2$ (CIGS) Nanocrystal (Inks) for Printable Photovoltaics," *J. AM. CHEM. SOC.* vol. 130, pp. 16770-16777, 2008. doi.org/10.1021/ja805845q.

[52] S. Averine, Y. C. Chan, and Y. L. Lam, "Evaluation of Schottky contact parameters in metal–semiconductor–metal photodiode structures**,"** *Appl. Phys. Lett.* vol. 77, pp. 274-276, 2000. doi.org/ 10.1063/1.126948.

[53] A. Luque, and S. Hegedus, *Handbook of photovoltaic and engineering*, United Kingdom: Wiley, p. 576, 2011.

[54] C. J. Panchal, M. S. Desai, V. A. Kheraj, K. J. Patel and N. Padha, "Barrier inhomogeneities in Au/CdSe thin film Schottky diodes**,"** *Semicond. Sci. Technol*. vol. 23, pp. 015003-015009, 2008. doi.org/10.1088/0268-1242/23/1/015003.

[55] P. J. Sellin, A. W. Davies, A. Lohstroh, M. E. Ozsan, and J. Parkin, "Drift Mobility and Mobility-Lifetime Products inCdTe:Cl Grown by the Travelling Heater Method," *IEEE transactions on nuclear science,* vol. 52, pp. 3074-3079, 2005. doi.org/10.1109/TNS.2005.855641.

[56] D. S. Ginger and N. C. Greenham, “Charge injection and transport in films of CdSe nanocrystals,” *J. Appl. Phys.* vol. 87, pp. 1361-1370, 2000. doi.org/10.1063/1.372021.

[57] I. Lokteva, N. Radychev, F. Witt, H. Borchert, J Parisi, and J. Kolny-Olesiak, “Surface Treatment of CdSe Nanoparticles for Application in Hybrid Solar Cells: The Effect of Multiple Ligand Exchange with Pyridine,” *J. Phys. Chem. C*. vol. 114, pp. 12784-12791 (2010). doi.org/10.1021/jp103300v.